Università degli Studi di Parma

TESI DI LAUREA SPECIALISTICA

Struttura e dinamica di sospensioni colloidali in equilibrio e fuori equilibrio mediante fotocorrelazione di radiazione X di sincrotrone (XPCS)

Structure and dynamics of equilibrium and non-equilibrium colloidal suspensions by means of synchrotron X-ray Photon Correlation Spectroscopy

Candidato:
Davide Orsi
Matricola 188511

Relatore:
Prof. Luigi Cristofolini

Correlatore:
Dott. Andrei Fluerasu

Anno Accademico 2007–2008

Contents

Sistemi colloidali: introduzione

Nella vita quotidiana, molti materiali non sono classificabili univocamente come solidi o liquidi, sia perché mostrano proprietà fisiche tipiche di entrambi questi stati della materia, sia perché il loro comportamento cambia sotto l'azione di forze esterne, o con il passare del tempo, oppure al variare della concentrazione o della temperatura. Questi sistemi, in fisica, sono comunemente denominati materia soffice. Tipicamente si tratta di miscele di due o più sostanze, tuttavia anche i sistemi polimerici e il vetro appartengono a questa categoria di materiali. Una caratteristica di questi sistemi è la viscoelasticità: a seconda dell'intensità della forza loro applicata, e della scala temporale considerata, si comportano come solidi oppure come liquidi, venendo deformati in modo irreversibile o reversibile, oppure ancora iniziando a scorrere.

Materiali molto diversi tra loro come vetri, emulsioni, paste, creme, gel e sabbia possono presentare le stesse proprietà, pur avendo strutture mesoscopiche molto diverse tra loro: sono microscopicamente disordinati ma possono agire come solidi cristallini da un punto di vista macroscopico. Questi materiali sono comunemente detti jammed appunto perché si comportano come solidi amorfi. Di fatto queste similitudini tra sistemi tanto diversi tra loro non sono accidentali, ma possono essere fatte risalire, in seguito ad una analisi più approfondita, a delle proprietà comuni. In generale, però, i comportamenti microscopici di sistemi jammed diversi mostrano pure notevoli differenze tra loro, e questa idea di una fisica comune non è stata ancora completamente dimostrata [1].

Nell'ambito della materia soffice, con sistemi colloidali ci si riferisce ad una sottoclasse costituita da sospensioni di particelle, con dimensioni dell'ordine o inferiori al micron, in un solvente liquido che può essere considerato come un mezzo continuo (figura 1). Molti prodotti alimentari fanno parte di questa categoria, come salse e latte, e altri materiali di uso comune come vernici, cosmetici o lubrificanti. Vi è anche un forte interesse teorico in questi materiali, poiché le sospensioni colloidali sono sistemi modello per lo studio delle proprietà termodinamiche di sistemi atomici e di processi biologici particolarmente complessi, come il ripiegamento delle proteine, fondamentali per la vita. Ancora di più, i sistemi colloidali sono interessanti anche perché sono un sistema fisico per il quale è possibile verificare facilmente le previsioni teoriche elaborate dalla Fisica Statistica.

Possono essere utilizzate particelle di forma qualunque, e diversi tipi di interazione tra le particelle possono essere facilmente ottenuti attraverso forze elettriche, magnetiche o entropiche. Comunemente possono essere prodotte o acquistate a basso costo sfere, micelle, barre e vari altri tipi di particelle. Modelli teorici di sospensioni ideali di sfere dure predicono un comportamento di tipo gas ideale a bassa densità, il congelamento liquido-solido al diminuire della temperatura o anche stati fisicamente più interessanti come gel e vetri dove la dinamica è arrestata. Ciò spiega perché le sospensioni colloidali sono comunemente utilizzate come modello per lo studio di sistemi dinamicamente arrestati: le transizioni di fase possono essere facilmente indotte variando parametri quali concentrazione, temperatura, pH della soluzione e, pertanto, le previsioni possono essere facilmente verificate attraverso gli esperimenti. Anche vari sistemi biologici possono essere modellizzati per mezzo di tali sospensioni, riproducendo processi di invecchiamento o di self-assembly.

Delle particelle sospese in un liquido possono formare aggregati, a causa di vari tipi di forze attrattive intermolecolari. Al fine di eliminare le interazioni che portano all'aggregazione, le particelle vengono modificate mediante processi detti di stabilizzazione. Essi sono principalmente di due tipi, illustrati nella figura 2:

Figura 1: Nanoparticelle d'oro sospese in acqua; il raggio delle particelle determina il colore della sospensione. Da [2].

- stabilizzazione di carica; attraverso l'azione di un solvente polare, una carica elettrica si accumula sulla superficie delle particelle, mentre ioni di carica opposta sospesi nel liquido formano un ulteriore strato esterno alla particella. Quindi, quando due di queste particelle si avvicinano, l'interazione coulombiana genera repulsione;

- stabilizzazione attraverso forze entropiche; quando uno strato di catene polimeriche circonda le particelle la vicinanza di queste ultime è termodinamicamente sfavorita, in quanto la conseguente compenetrazione dei layer polimerici di due diverse particelle corrisponderebbe ad una diminuzione dell'entropia.

Nel primo caso, abbiamo un'interazione a lungo raggio. Utilizzando il secondo metodo, invece, si ottiene un'interazione a corto raggio che riproduce una parete di potenziale infinita: le particelle si comportano come sfere dure.

Particelle di silice in acqua o in glicerolo sono un esempio ben noto di sistema stabilizzato mediante carica elettrica, mentre sfere di PMMA rivestite con polimeri e sospese in decalina, costituenti il principale campione esaminato in questo studio, sono un paradigma di una sospensione stabilizzata da forze entropiche.

Come la concentrazione sale, le forze attrattive aumentano portando alla formazione di un gel: questo di solito accade quando la frazione di volume
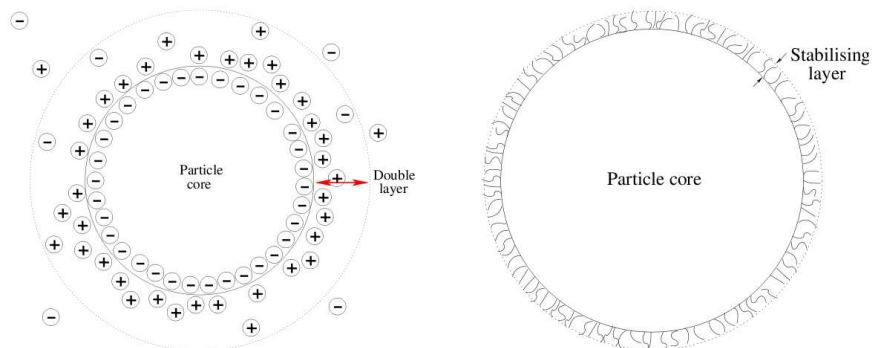
Figura 2: Stabilizzazione di particelle colloidali. Sinistra: stabilizzazione di carica; Destra: stabilizzazione mediante forze entropiche. Da [3].

è superiore al $50 - 60\%$. Questo processo viene chiamato flocculazione, - aggregazione o gelificazione, e può verificarsi se il campione non è conservato con cura. Ad esempio, se il contenitore è lasciato aperto nel corso di una misurazione, il solvente evapora distruggendo l'invarianza temporale.

Microfluidica applicata agli esperimenti con radiazione X

Il termine microfluidica indica un gruppo di tecniche sperimentali che implicano l'uso di siringhe e tubi (con un raggio che va da $1\mu m$ fino a $1mm$) per fare fluire il campione nel corso dell'esperimento, a volte mescolando i vari componenti del campione direttamente nel tubo, subito prima della misura. Ci sono diverse ragioni, nello studio della materia soffice, per avere il campione che fluisce in un tubo invece di contenerlo in un capillare o in una provetta:

- evitare effetti spuri, dati da cavitazione e da altre modificazioni indesiderate delle proprietà del sistema indotte dal forte fascio di raggi X,
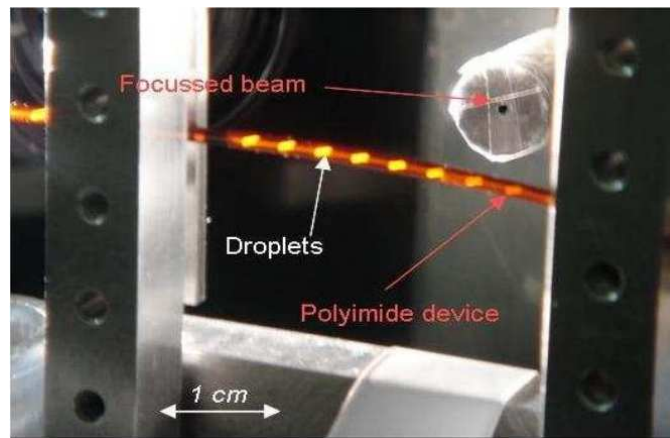
Figura 3: Esperimento di microfluidica: gocce di campione scorrono in un flusso di olio.

fornendo continuamente nuovo campione; sono necessari solamente una siringa e un tubo.

- misurare facilmente con i trascorrere del tempo processi come gelificazione, reazioni chimiche o transizioni di fase con un semplice apparato sperimentale; utilizzando una siringa per ogni componente e connessioni a T è possibile mescolare il campione direttamente nel tubo, definendo questo istante come $t_0 = 0s$. In questo modo la distanza tra il punto di miscelazione e la posizione del fascio è direttamente legata al tempo trascorso t_1;

- misurare le proprietà di un campione confinato in un volume ristretto creando gocce di campione (ad esempio una sospensione colloidale, figura 3) che scorrono in un mezzo liquido (ad esempio olio); per realizzare una configurazione adatta allo scopo sono necessarie almeno due siringhe, una per l'olio e una per il campione, connesse a due tubi disposti uno dentro l'altro.

Tutti questi diversi tipi di risultati può essere raggiunti utilizzando componenti, come tubi e siringhe, poco costose e facili da reperire. Tuttavia, un

punto importante da discutere è fino a che punto la presenza del flusso modifica la dinamica intrinseca delle particelle studiate. Il presente lavoro di tesi affronta questo punto. La risposta ottenuta è molto semplice: in condizioni sperimentali ragionevoli, la presenza del flusso non influenza le proprietà dinamiche osservate se il momento scambiato $\vec{Q}$ è perpendicolare alla direzione del flusso. L'uso di questo tipo di configurazione, chiaramente, facilita la realizzazione pratica di tali esperimenti.

Risultati sperimentali

Struttura di sospensioni di sfere dure

Dopo una prima caratterizzazione della sospensione colloidale considerata, costituita da sfere dure di PMMA in decalina, avendo misurato la sua viscosità e il coefficiente di diffusione di Einstein-Stokes D_0, abbiamo iniziato l'analisi della sue proprietà statiche e dinamiche in funzione della concentrazione di particelle, misurata come frazione di volume Φ. La caratterizzazione della struttura del campione è stata effettuata mediante SAXS (Small Angle X-ray Scattering) presso le beamline ID10A e ID02 di ESRF: il nostro primo obiettivo consiste nel conoscere esattamente che tipo di sospensione stiamo esaminando. Come illustrato nel capitolo 2.1, infatti, la distribuzione delle dimensioni delle particelle e la volume frazione della sospensione sono entrambe misurabili attraverso questa tecnica.

Durante la preparazione del campione, particolare cura è stata posta nell'evitare qualsiasi alterazione del valore medio e della deviazione standard del raggio delle particelle. La preparazione di campioni ad alta concentrazione mediante centrifugazione può portare alla presenza di un gradiente di dimensioni nel sedimento: di conseguenza, durante la successiva eliminazione del solvente presente in superficie, le particelle più piccole possono essere accidentalmente eliminate. Pertanto, la centrifugazione non è stato utilizzata nel corso della preparazione dei campioni.

Come rivelatore abbiamo utilizzato un sensore CCD, in virtù del grande intervallo di momento trasferito studiato con un'unica immagine e dell'al-

ta risoluzione: con una scelta giudiziosa della distanza campione-rivelatore $(d = 2.19m)$ è possibile eseguire misure in una regione di Q che va da $Q \simeq 0.001 \mathring{A}^{-1}$ fino a $Q \simeq 0,03 \mathring{A}^{-1}$.
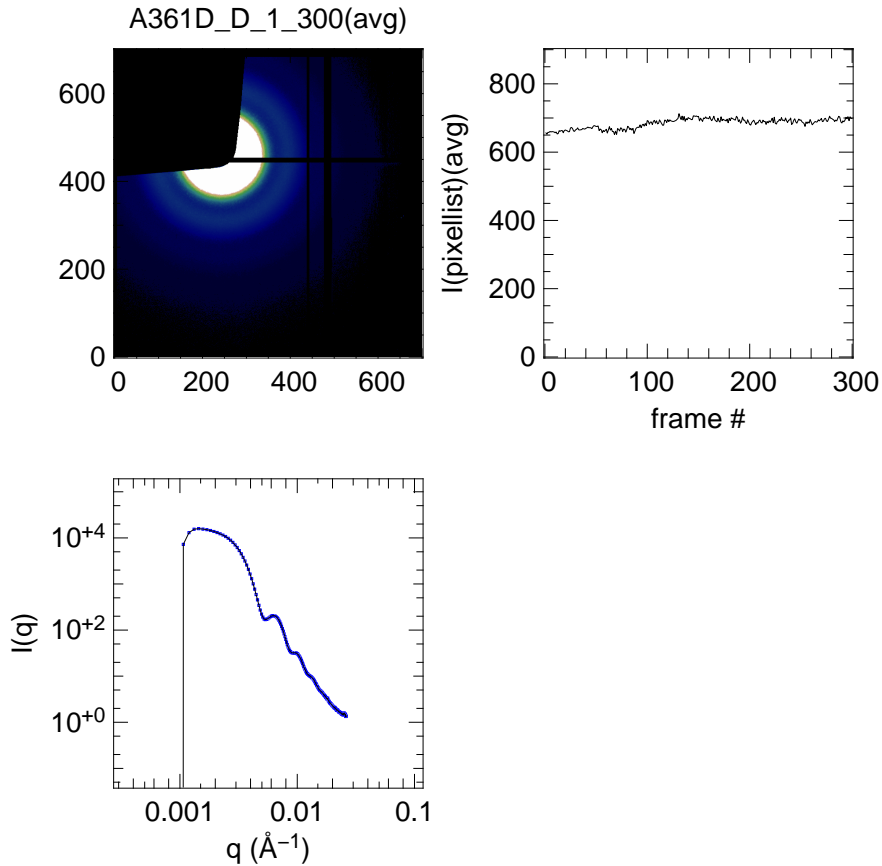

Figura 4: Misura SAXS. In alto a sinistra: vengono misurate 300 immagini, quindi si calcola la loro media. In alto a destra: intensità media in funzione del tempo. In basso: media radiale dell'intensità in funzione di Q.

Un piccolo pezzo di metallo sagomato, detto beamstop, è interposto tra il fascio X e il rivelatore, impedendo il danneggiamento di quest'ultimo. Dato che il limite inferiore di Q è determinato dalla posizione del beamstop rispetto al fascio diretto, a volte la misurazione non raggiunge valori Q sufficientemente piccoli rendendo impossibile ottenere informazioni sulla struttura del campione. In questi casi, abbiamo integrato i dati con quelli misurati utilizzando un fototubo, anche se in questo caso la risoluzione è inferiore. Utiliz-

zando il CCD (figura 4), normalmente vengono raccolti 300 fotogrammi al fine di compensare il limitato range dinamico del detector. Le immagini sono state poi sommate insieme pixel per pixel, ottenendone una unica. Una media radiale viene eseguita attorno al punto dove incide il fascio, che si ottiene misurando una immagine senza beamstop ma con alcuni attenuatori inseriti nel percorso del fascio. I pixel difettosi sono stati mascherati, e una misura effettuata senza fascio è stata sottratta ai dati ottenuti al fine di eliminare eventuali effetti spuri. L'intensità di radiazione diffusa in funzione di Q ottenuta in questo modo può essere fittata con i modelli descritti nel capitolo 2.1, i quali danno accesso a tutti i parametri che descrivono il campione da un punto di vista statico come il raggio e la concentrazione, ottenendo inoltre una misura del fattore di struttura $S(Q)$, che sarà utile nelle analisi successive. L'importanza di questo fattore, contenente informazioni sulle interazioni interparticellari, aumenta con il crescere della frazione di volume Φ, mentre è praticamente uguale a uno a basse concentrazioni.

Non è ancora possibile, tuttavia, confrontare direttamente i risultati del nostro esperimento con il modello teorico, in quanto è necessario sottrarre il contributo alla diffusione dovuto sia il solvente che ai tubi di kapton. Inoltre, è necessario tenere conto dell'influenza della risoluzione strumentale sulla misura dell'intensità $I(Q)$. Per fare ciò, in letteratura solitamente si esegue una convoluzione del fattore di forma di una sfera dura con una curva Gaussiana, di larghezza pari all'incertezza del momento trasferito, e quindi all'incertezza dell'energia dei fotoni incidenti.

I dati sono stati fittati con l'espressione, riportati nel capitolo 2.1,

$$I(Q) = K\, S(Q)\, P(Q) \tag{1}$$

dove K è un fattore di scala, $P(Q)$ è il fattore di forma di una sfera e $S(Q)$ è il fattore di struttura. Il valore medio $\overline{R}$ e la deviazione standard $\sigma = \overline{R}/\sqrt{Z+1}$ del raggio R delle particelle sono i parametri del fit, mentre la frazione di volume del campione Φ è un parametro variato manualmente. La determinazione del fattore di struttura è il principale obiettivo di questa misura: esso può essere ottenuto calcolando il rapporto tra $I(Q)$ e il fattore

11

di forma riscalato $K P(Q)$, convoluto con un profilo gaussiano per tenere conto della presenza di un'incertezza nella determinazione dell'energia dei fotoni incidenti, e quindi nella determinazione di Q. Possiamo chiamare la grandezza così ottenuta fattore di struttura misurato. Questa curva può essere paragonata con la curva $S(Q)$ prevista, nell'approssimazione Percus-Yevich, per particelle sferiche che interagiscono come sfere dure.

Un altro modello che potrebbe essere usato durante l'analisi è l'espressione di $I(Q)$, riportata in [4], dove non si ha fattorizzazione nei due fattori $S(Q)$ e $P(Q)$: un fit eseguito usando questo modello non consente la determinazione del fattore di struttura, anche se R e Φ possono essere determinati con maggiore precisione.

Nelle figure 5a, 6a, 7a, 8a, 9a, 10a and 10a sono riportati le misure SAXS e i relativi fit relativi a campioni caratterizzati da una frazione di volume pari fino a circa il 50%. Le figure 5b, 6b, 7b, 8b, 9b, 10b and 11b riportano i fattori di struttura misurato e previsto.
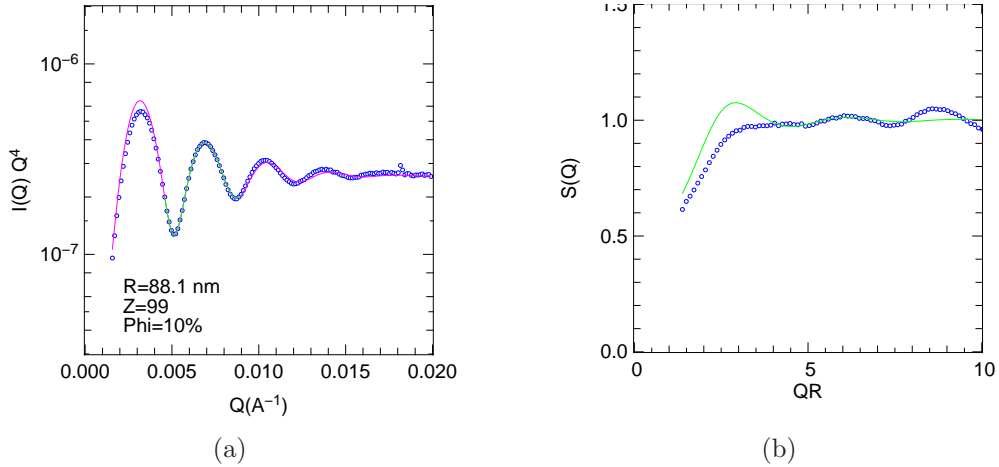

Figura 5: A631D_D. a) Dati fittati solamente nella regione verde, con $R = (881 \pm 3)\mathring{A}$; $Z = 99 \pm 6$; $\Phi = 9.5\%$; b) Fattore di struttura: i punti indicano il fattore di struttura misurato, la curva continua quello atteso.

(a)

(b)

Figura 6: A631D_C. a) Dati fittati solamente nella regione verde, con $R = (893 \pm 3)\mathring{A}$; $Z = 105 \pm 6$; $\Phi = 19.5\%$; b) Fattore di struttura: i punti indicano il fattore di struttura misurato, la curva continua quello atteso.
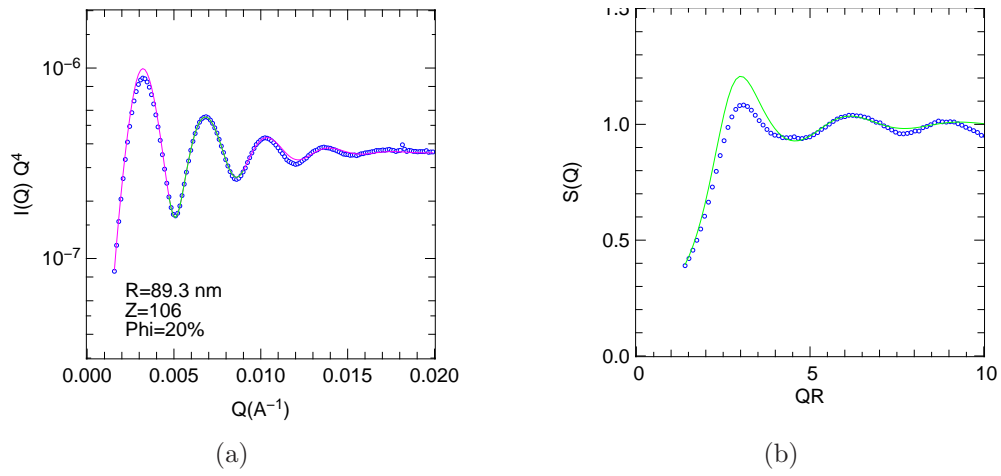

(a)

(b)

Figura 7: A631D_E. a) Dati fittati solamente nella regione verde, con $R = (908 \pm 3)\mathring{A}$; $Z = 99 \pm 4$; $\Phi = 21.5\%$; b) Fattore di struttura: i punti indicano il fattore di struttura misurato, la curva continua quello atteso.

Figura 8: A631D_P. a) Dati fittati solamente nella regione verde, con $R = (905 \pm 3)\mathring{A}$; $Z = 107 \pm 4$; $\Phi = 30.5\%$; b) Fattore di struttura: i punti indicano il fattore di struttura misurato, la curva continua quello atteso.
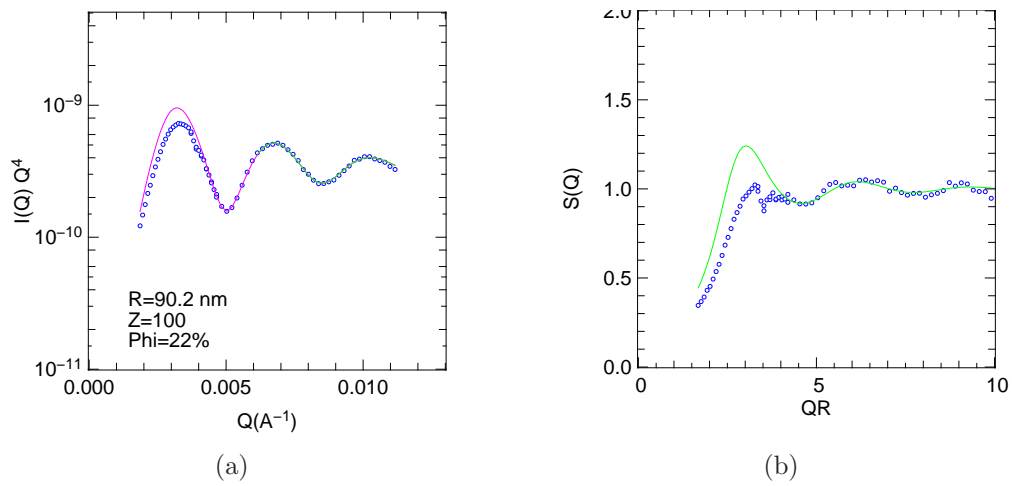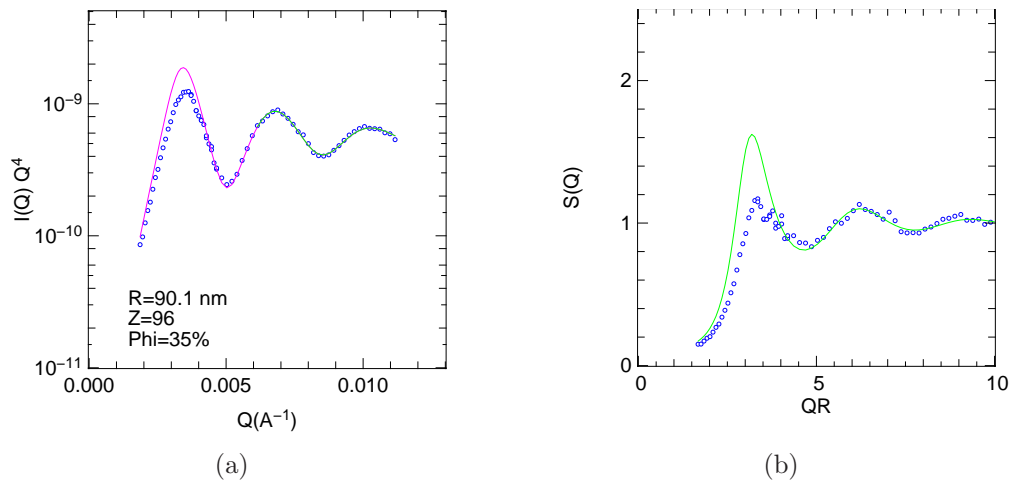

Figura 9: A631D_F. a) Dati fittati solamente nella regione verde, con $R = (901 \pm 3)\mathring{A}$; $Z = 96 \pm 2$; $\Phi = 35.2\%$; b) Fattore di struttura: i punti indicano il fattore di struttura misurato, la curva continua quello atteso.
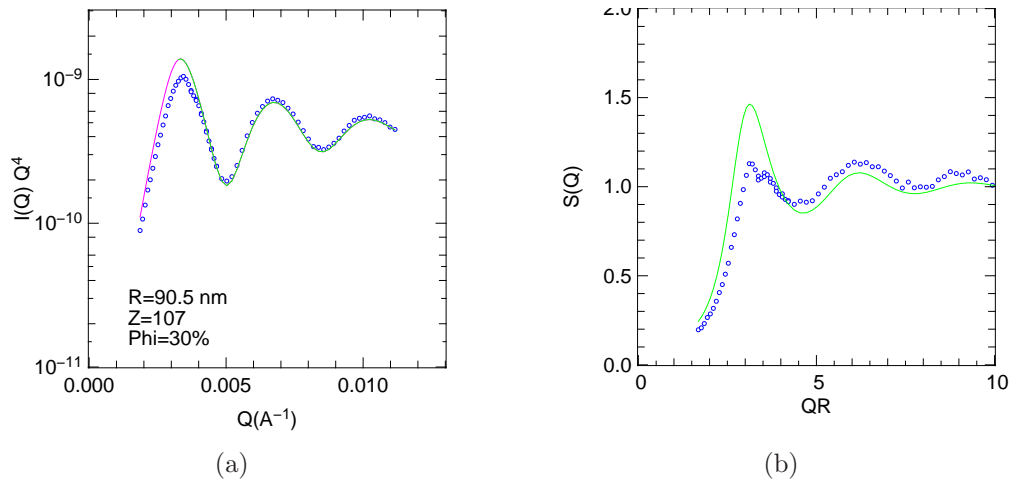
Figura 10: A631D_A. a) Dati fittati solamente nella regione verde, con $R = (901 \pm 3)\mathring{A}$; $Z = 90 \pm 5$; $\Phi = 44\%$; b) Fattore di struttura: i punti indicano il fattore di struttura misurato, la curva continua quello atteso.

Figura 11: A631D_G. a) Dati fittati solamente nella regione verde, con $R = (896 \pm 5)\mathring{A}$; $Z = 84 \pm 8$; $\Phi = 50.5\%$; b) Fattore di struttura: i punti indicano il fattore di struttura misurato, la curva continua quello atteso.
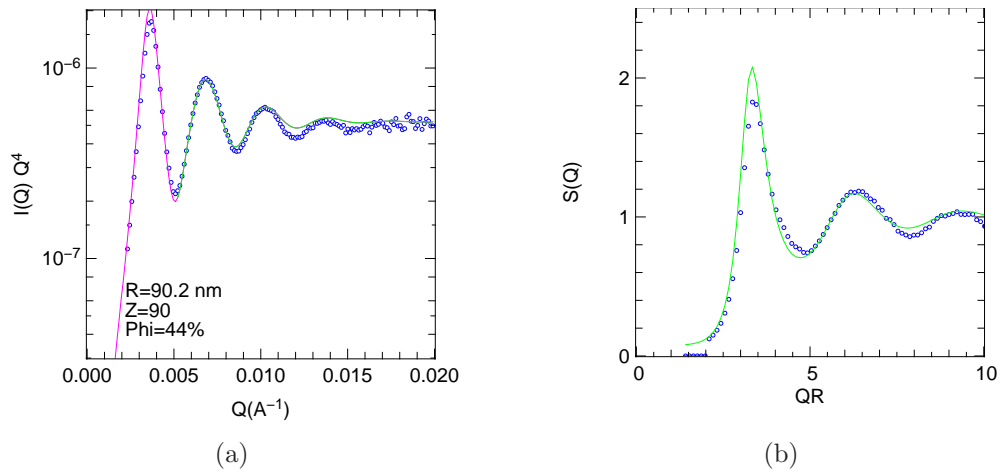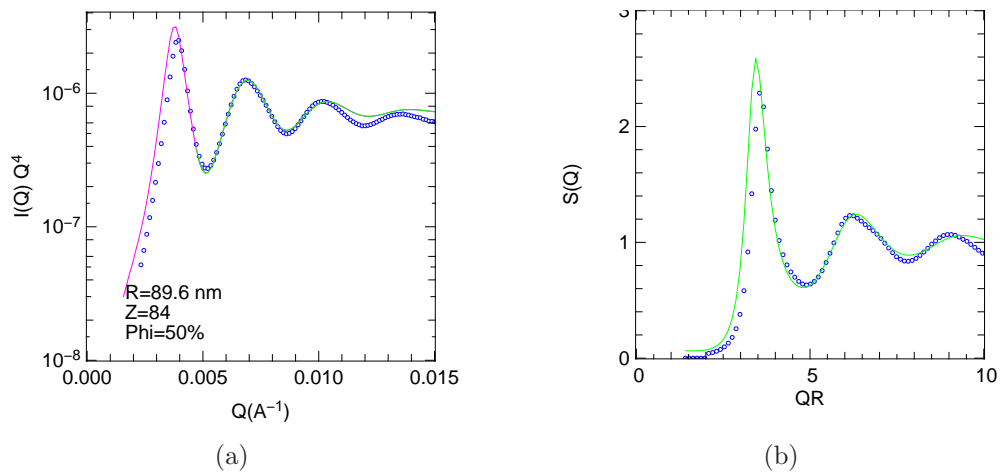
15

Come si può vedere, il fit è migliore nella regione dove il momento trasferito è elevato, mentre ci sono alcuni problemi nella regione a piccoli Q. Il problema è che la curva teorica riesce a descrivere bene solo una delle due regioni. Il nostro tentativo di superare questo problema operando una convoluzione del modello con una gaussiana per tenere conto della risoluzione in energia non è sufficiente. Effettuando il fit nella regione $Q > 0.005 \mathring{A}^{-1}$ si ottiene un valore errato dell'intensità del picco di struttura. D'altro canto, cercando di ottenere un fit migliore nella regione a piccolo Q porta a cattivi risultati per la restante parte della curva; è pertanto necessario un approccio equilibrato. Abbiamo deciso di limitare il fit solo ai primi due massimi dell'intensità che seguono il picco di struttura. Dato che nell'analisi seguente alcune delle principali informazioni di cui avremo bisogno sono le posizioni dei massimi, e dato che possiamo accettare qualche discrepanza nella determinazione delle intensità, abbiamo cercato di ottenere dei valori di media e deviazione standard del raggio delle sfere compatibili tra tutti i campioni. I valori della concentrazione ricavati dal fit sono compatibili con i valori previsti.

sample	nominal Φ	Φ	R ($\mathring{A}$)	Z	σ ($\mathring{A}$)
A361D_D	10%	9.5%	881 ± 3	99 ± 6	88 ± 3
A361D_C	19%	19.5%	893 ± 3	105 ± 6	86 ± 3
A361D_E	22%	21.5%	908 ± 3	99 ± 4	90 ± 2
A361D_F	30%	30.5%	905 ± 3	107 ± 4	87 ± 2
A361D_P	35%	35.2%	901 ± 3	96 ± 2	91 ± 2
A361D_A	45%	44%	901 ± 3	90 ± 5	94 ± 3
A361D_G	50%	50.5%	896 ± 5	84 ± 8	97 ± 5

Abbiamo ottenuto un fattore di struttura misurato diverso dalla previsione teorica per una sospensione di sfere dure ottenuta dall'approssimazione di Percus-Yevich. Ciò è probabilmente un'indicazione che tale modello non è applicabile al nostro sistema, anche se una spiegazione alternativa potrebbe essere correlata a problemi sperimentali a bassi valori di Q. In ogni caso, una prova che il nostro campione è effettivamente fatto di sfere deriva dal

confronto del raggio ottenuto dal fit con il cosiddetto raggio idrodinamico $R_h = \frac{k_B T}{6\pi\eta D_0}$. Nel caso del nostro campione, $R_h \simeq 930$ Å: dal momento che questo valore è leggermente superiore al valore medio di R ricavato dal fit dei dati SAXS, il nostro campione probabilmente non contiene sfere rotte o altre particelle non sferiche.

Dinamica di sospensioni di sfere dure

La seconda parte di questo lavoro è focalizzata sulla dinamica delle particelle e sulle interazioni interparticellari. Poiché stiamo eseguendo misurazioni in una regione dello spazio reciproco dove $QR < 10$, stiamo principalmente prendendo in considerazione le interazioni tra particelle separate da una distanza $d > \frac{2\pi R}{10} = 0.6R \simeq 60nm$. La dinamica delle nanoparticelle in un mezzo continuo presenta tre diversi regimi:

- il regime balistico, se si considera un tempo abbastanza breve da poter considerare le particelle colloidali, dopo una collisione, come particelle libere;

- il regime browniano a tempi brevi, quando la particella si muove attorno alla sua posizione di equilibrio: in questo caso il moto è diffusivo e non è stato rallentato da interazioni interparticellari;

- il regime diffusivo a tempi lunghi, quando la particella si muove su distanze maggiori ed il suo movimento è influenzato dal cosiddetto effetto gabbia dovuto alla presenza delle particelle circostanti.

Questo lavoro è focalizzato solo sul regime a tempi brevi. La separazione tra i vari regimi è data ovviamente dalla scala temporale che caratterizza la diffusione, e dal suo confronto con alcune costanti di tempo definite da alcuni parametri statici come raggio (R) e massa (m) delle particelle, temperatura (T) e viscosità (η). Possiamo definire due costanti di tempo particolarmente rilevanti:

- la prima, $\tau_B = mD_0/k_BT \simeq 1ns$, è il cosiddetto tempo di rilassamento browniano: questo è il tempo necessario ad una particella, dopo una collisione, per perdere un'energia comparabile con l'energia di eccitazione termica k_BT interagendo con il solvente. Pertanto, questo è il tempo dopo il quale ha significato definire il coefficiente di diffusione;

- la seconda costante di tempo è pari al tempo che necessita ad una particella per diffondere liberamente su una distanza pari al suo raggio, e può dunque essere definito come $\tau_R = R^2/D_0 \simeq 9ms$.

Quando $\tau_B < \tau < \tau_R$ si ha il regime a tempi brevi, il regime a tempi lunghi si verifica quando $\tau > \tau_R$. Lo studio del regime balistico non è possibile mediante XPCS, in quanto rivelatori in grado di raggiungere tempi di misura inferiori a τ_B non sono disponibili. In breve, stiamo osservando la dinamica e le interazioni tra particelle separate da distanze di gran lunga maggiori rispetto al loro raggio che hanno luogo durante un tempo più breve del tempo necessario ad una particella per diffondere su una distanza comparabile con il suo raggio.

La misura delle funzioni di correlazione mediante XPCS è stata eseguita a diversi valori di Q, corrispondenti ad una regione che arriva fino al secondo massimo del fattore di struttura, ossia dove $QR < 6$. Da un lato, in campioni con concentrazione molto bassa la funzione di correlazione è un decadimento esponenziale:

$$g^{(2)}(\tau) = 1 + \left| \frac{F(\vec{Q},t)}{F(\vec{Q},0)} \right|^2 = 1 + e^{-2D_0Q^2t}.$$

dove D_0 è il coefficiente di diffusione di Einstein-Stokes.

D'altro canto, a concentrazioni più elevate, questa espressione non è più valida: è necessario introdurre una dipendenza da Q nel coefficiente di diffusione $D_S(Q)$. Se si riporta in scala semi-logaritmica, come in figura 12, una funzione di correlazione misurata a una concentrazione elevata, possiamo vedere che essa presenta due diverse scale temporali. Questo richiama la presenza dei due diversi regimi di diffusione, precedentemente denominati a
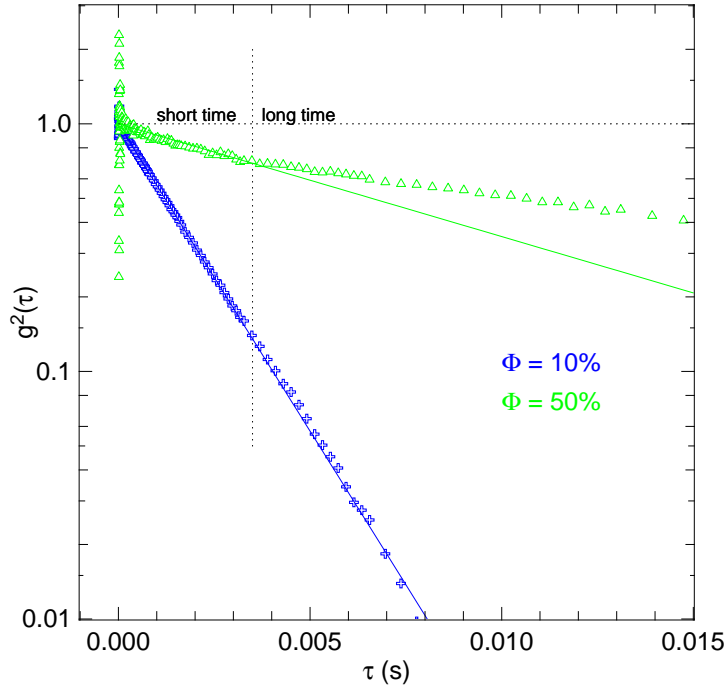
Figura 12: Funzioni di correlazione a $\Phi = 10\%$ e a $\Phi = 50\%$. Nella curva con Φ elevato, sono chiaramente visibili due scale temporali: il fit è eseguito solamente sulla regione a tempi brevi.

tempi brevi e a tempi lunghi, separati dal tempo caratteristico τ_R. Pertanto, attraverso un fit esponenziale sui dati nella regione $\tau < \tau_R$ si ottiene una misura di $D_S(Q)$. Questa misura è stata eseguita a diverse velocità del flusso di campione, che vanno da zero fino a $800\mu L/h$ e anche $1600\mu L/h$. Se i dati ottenuti per piccoli valori della velocità di flusso sono compatibili con quelli misurati senza flusso, non sono presenti né cavitazione né effetti di ageing. Inoltre, se i dati misurati a bassi valori della velocità di flusso sono coerenti l'uno con l'altro, mentre la curva a flusso zero mostra un comportamento diverso, ciò significa che questa ultima non è completamente affidabile. Velocità di flusso eccessive comportano la presenza nelle funzioni di correlazione di effetti indotti dal flusso stesso, e non sono quindi adatti per le successive analisi.

Nel corso dell'analisi di $D_S(Q)$, è utile mettere da parte il contributo delle interazioni dirette, rappresentato dal fattore di struttura $S(Q)$ che abbiamo ottenuto attraverso la misura SAXS. Dal momento che si osservano i moti delle particelle su tempi più brevi del tempo τ_R necessario alle sfere per diffondere su una distanza pari al loro raggio, possiamo considerare le nanoparticelle come in moto attorno alle loro posizioni di equilibrio. In questa situazione, effetti strutturali e idrodinamici possono essere separati fattorizzando $D_S(Q)/D_0$, come suggerito in [5]:

$$\frac{D_S(Q)}{D_0} = \frac{H(Q)}{S(Q)} \qquad (2)$$

D_0 è stato misurato mediante DLS, $S(Q)$ mediante SAXS e $D_S(Q)$ mediante XPCS; abbiamo ricavato una misurazione della cosiddetta funzione idrodinamica $H(Q)$, rappresentante l'interazione interparticellare mediata dal movimento del solvente come effetto del movimento delle altre particelle e della particella stessa.
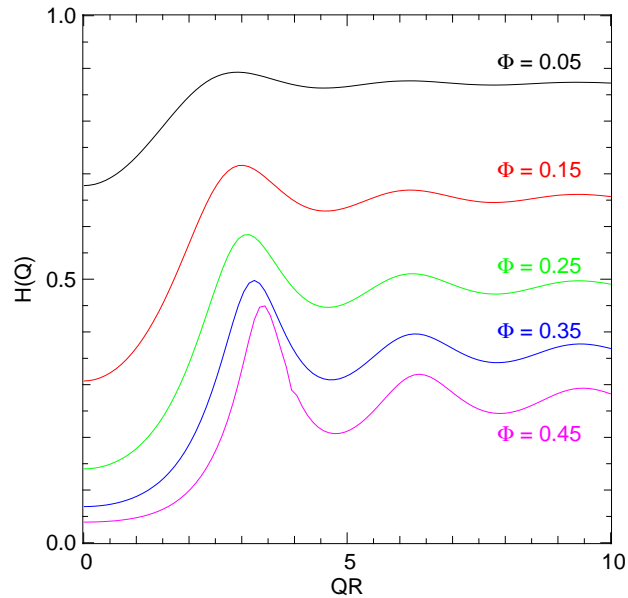

Figura 13: Previsione teorica dell'andamento della funzione idrodinamica a varie concentrazioni.

Un modello per $H(Q)$ in funzione della frazione di volume della sospensione è stato sviluppato da Beenakker e Mazur: nell'articolo [6] hanno studiato il contributo dovuto al moto della stessa particella in esame, che dà luogo ad un termine indipendente da Q, mentre in [7] si sono prese in considerazione interazioni idrodinamiche a molti corpi, che danno invece origine ad un contributo dipendente da Q. Il calcolo è lungo e abbastanza complicato, e non è riportato qui: comunque, l'espressione finale di $H(Q)$ richiede una integrazione numerica che è stata eseguita come parte dei compiti del presente lavoro di tesi. I risultati sono riportati in figura 13, simile alla figura 2 riportata in [7].
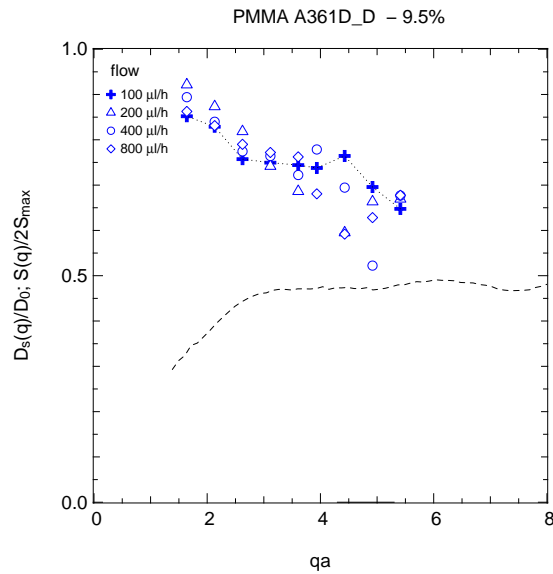

Figura 14: A361D_D, $\Phi = 9.5\%$. Viene riportato $D_S(Q)$ normalizzato a D_0 in funzione del momento trasferito. Anche il fattore di struttura $S(Q)$ misurato è riportato per un rapido confronto.

Figura 15: A361D_C, $\Phi = 19.5\%$. Viene riportato $D_S(Q)$ normalizzato a D_0 in funzione del momento trasferito. Anche il fattore di struttura $S(Q)$ misurato è riportato per un rapido confronto.

Figura 16: A361D_E, $\Phi = 21.5\%$. Viene riportato $D_S(Q)$ normalizzato a D_0 in funzione del momento trasferito. Anche il fattore di struttura $S(Q)$ misurato è riportato per un rapido confronto.
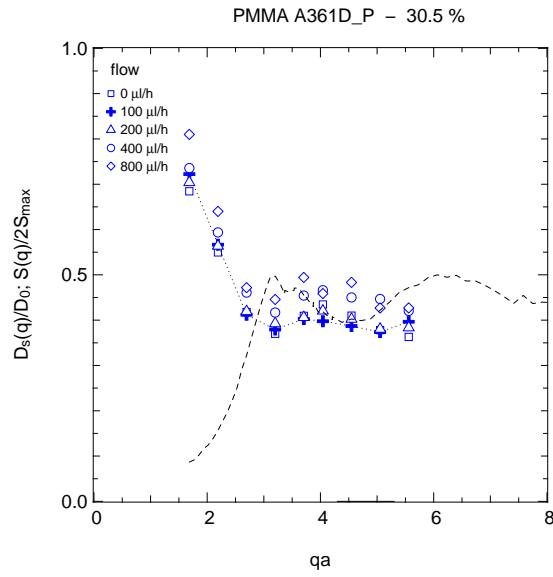
Figura 17: A361D_P, $\Phi = 30.5\%$. Viene riportato $D_S(Q)$ normalizzato a D_0 in funzione del momento trasferito. Anche il fattore di struttura $S(Q)$ misurato è riportato per un rapido confronto.
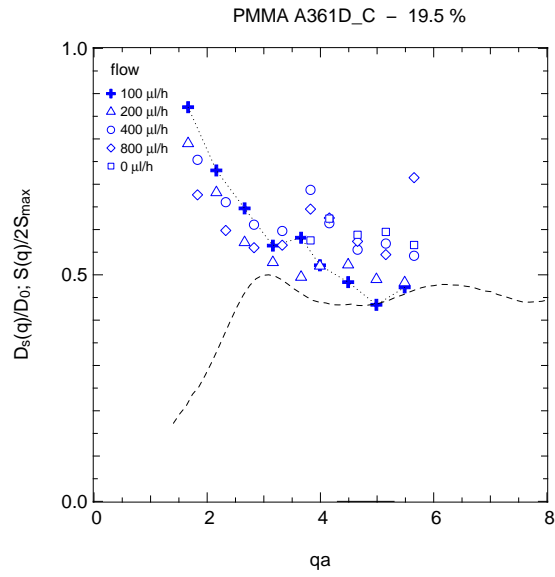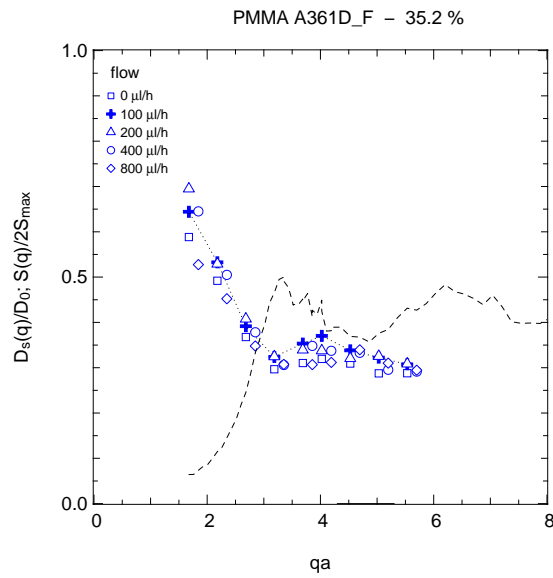

Figura 18: A361D_F, $\Phi = 35.2\%$. Viene riportato $D_S(Q)$ normalizzato a D_0 in funzione del momento trasferito. Anche il fattore di struttura $S(Q)$ misurato è riportato per un rapido confronto.
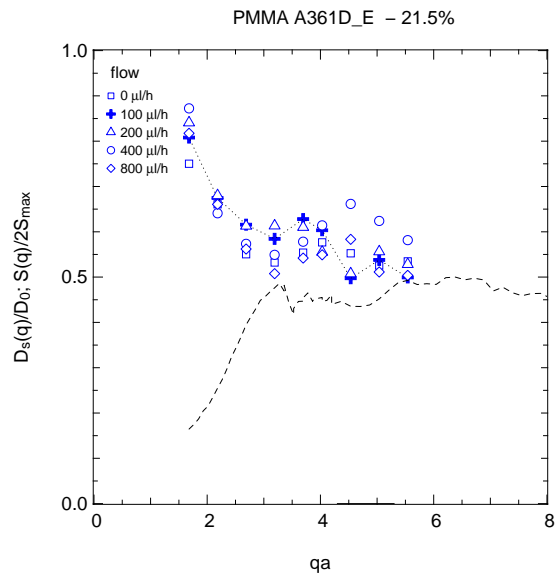
Figura 19: A361D_A, $\Phi = 44.0\%$. Viene riportato $D_S(Q)$ normalizzato a D_0 in funzione del momento trasferito. Anche il fattore di struttura $S(Q)$ misurato è riportato per un rapido confronto.

Figura 20: A361D_G, $\Phi = 50.5\%$. Viene riportato $D_S(Q)$ normalizzato a D_0 in funzione del momento trasferito. Anche il fattore di struttura $S(Q)$ misurato è riportato per un rapido confronto.
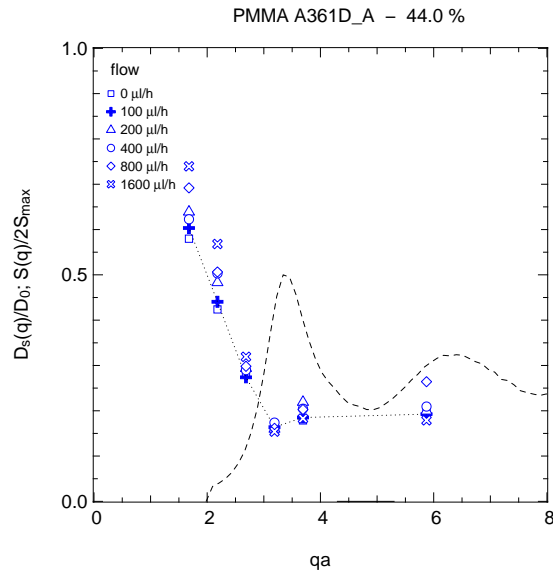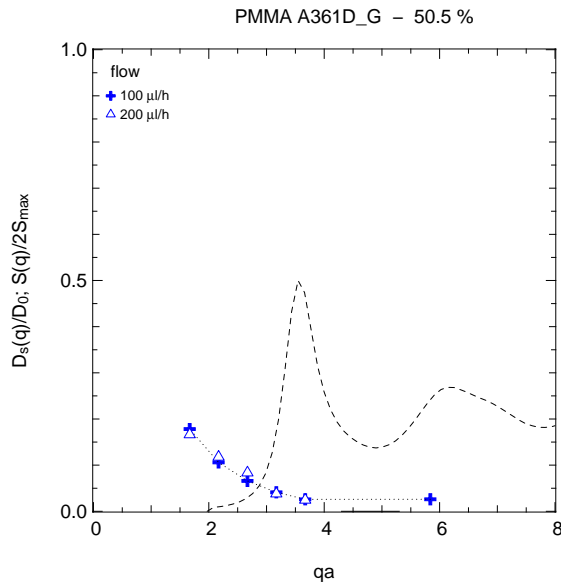
Risultati

Nelle figure dalla 14 alla 20, ciascuna riferita a un diverso campione, viene riportata la funzione $D_S(Q)$ normalizzata al coefficiente di Einstein-Stokes, così come il corrispondente fattore di struttura. Sono stati evidenziati i dati misurati con il campione che scorreva a $100\mu L/h$, poiché tale velocità di flusso soddisfa i requisiti riportati sopra: cavitazione e effetti di invecchiamento indesiderati sono completamente assenti.

Si noti che in ogni figura il primo minimo relativo corrisponde alla posizione del massimo di S(Q), in posizione Q_{max}: la dinamica misurata in corrispondenza del picco di struttura è più lenta. Le fluttuazioni di densità della sospensione con lunghezza d'onda $\frac{2\pi}{Q}$ decadono in modo esponenziale, ad eccezione di quelle con una lunghezza d'onda paragonabile a $\frac{2\pi}{Q_{max}}$ che paiono invece persistere: il loro decadimento avviene con un tempo caratteristico più grande. Questo effetto è molto simile al de Gennes narrowing, effetto ben noto in letteratura [8]. Esso consiste in un restringimento in energia dell'intensità di neutroni diffusi quasielasticamente in funzione del momento trasferito Q in corrispondenza del massimo del fattore di struttura $S(Q)$. L'origine fisica di questo effetto giace nel fatto che la dinamica del sistema tende a rallentare in corrispondenza di eventuali periodicità; in altre parole, il sistema tende a preservare la sua coerenza a quel particolare valore di Q rallentando la dinamica corrispondente.

Come si può vedere nelle figure 14 e 15, i campioni a bassa concentrazione A361D_D e A361D_C mostrano problemi di dispersione dei dati tra le curve relative a velocità di flusso diverse. In particolare, non è presente un andamento oscillante comune nei dati relativi ad ogni velocità di flusso, mentre i campioni con concentrazione superiore non presentano questo problema. In questi ultimi le oscillazione di $S(Q)$ e $D_S(Q)$ sono in chiaro accordo. Per questo motivo il campione A361D_C non è stato considerato nel corso dell'analisi della funzione idrodinamica $H(Q)$, dal momento che la sua concentrazione $\Phi \simeq 19\%$ è molto simile a quella del campione A361D_E, $\Phi \simeq 21\%$.

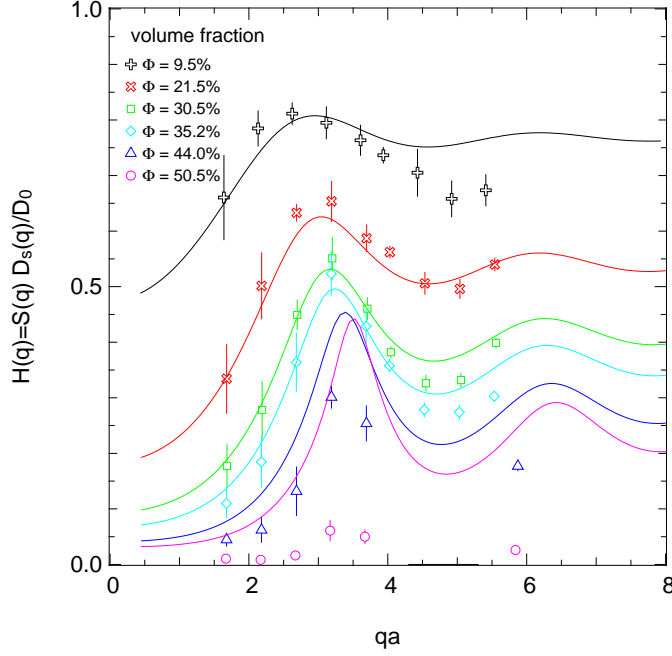Possiamo ora calcolare la funzione idrodinamica $H(Q)$ introdotta dal-

Figura 21: $H(Q)$ a varie concentrazioni. Le linee continue rappresentano le previsioni teoriche di Beenakker e Mazur. Le barre d'errore derivano dall'analisi statistica delle funzioni di correlazione (capitolo 3.2) e dei fattori di struttura $S(Q)$.

l'espressione (2) per rappresentare ogni altro contributo al coefficiente di diffusione, in particolare le interazioni mediate attraverso il solvente liquido, chiamate interazioni idrodinamiche. Nella figura 21 sono riportati i dati misurati a diverse concentrazioni con una velocità di flusso di $100\mu L/h$. L'unica eccezione è costituita dal campione A361D_E poiché, anche se si tratta di un campione a bassa concentrazione in linea di principio non soggetto a problemi di cavitazione, per esso si ha che la curva misurata a $100\mu L/h$ presenta una dipendenza da Q non compatibile con i dati misurati a flusso nullo. Per il campione A361D_E sono stati utilizzati i dati misurati a campione fermo.

I valori di $H(Q)$ sono stati confrontati le curve teoriche calcolate per i rispettivi valori di R, Z e Φ, sulla base delle equazioni riportate in [6] e in [7]. Risulta evidente come a bassa concentrazione la funzione idrodinamica

teorica sia non strutturata, mentre ad alte frazioni di volume la curva teorica $H(Q)$ presenta un primo massimo a $QR \simeq 3$ e un successivo minimo a $QR \simeq 4.5$; questo comportamento è ragionevolmente ben riprodotto dai nostri dati sperimentali. A $\Phi = 44\%$, la dinamica del campione comincia ad arrestarsi, infatti è possibile vedere una chiara deviazione dei dati dal comportamento previsto. A $\Phi = 50\%$ il campione non è più fluido ma appare più come un gel; ovviamente, applicare ad un gel una teoria sviluppata per le particelle in sospensione in un liquido porta a conclusioni teoriche completamente errate.

Chapter 1

Introduction: colloidal systems in soft matter

In everyday life, there is a great variety of materials whose classification as solid or liquid systems is debatable, mainly because they show physical properties typical of both these states of matter, or because their behaviour under external forces changes either with time, concentration or temperature. These systems, in physics, are commonly referred to as "soft condensed matter". Typically, they consist of mixtures of two or more substances, although also polymers and glass belong to this category. One characteristic of these systems is viscoelasticity: depending on how strong the applied stress is, and on the time-scale involved, they behave like solids or like liquids and they can be deformed in either an irreversible or reversible way, or flow.

Very different materials like glasses, emulsions, pastes, creams, gels and sand may show the same properties, while having very different mesoscopic structures: they are microscopically disordered, yet acting like solids from a macroscopic point of view. These materials are usually referred to as "jammed" because they can act like amorphous solids. As a matter of fact these similarities are not accindental, but they can be traced back to deeper common properties. However, microscopic behaviours of "jammed" systems show great differences as well, and this idea of a common underlying physics

has not been completely proved yet [1].

Among soft condensed materials, "colloidal systems" is the name of a subclass that consists of a suspension of particles with micron or submicron size into a liquid solvent that can be considered as a continuous medium (figure 1.1). Many foods are part of this category, like sauces and milk, and other commonly used materials like paints, cosmetics or lubricants. There is also a strong theoretical interest in these materials since colloidal suspensions are good models to study the thermodynamical properties of atomic systems, protein folding and of other complex biological processes that are fundamental for life. But on top of that, colloids are interesting just because they are a real physical system that can used to test theoretical predictions in Statistical Physics.

Different particle shapes can be provided, and different kinds of interaction among particles can be easily achieved through electric, magnetic or entropic interactions. Commonly spheres, rods, micelles, core-shell particles can be produced or bought at low costs. Theoretical models of hard-spheres suspensions predict ideal-gas behaviour at low density, liquid-solid freezing or more physically interesting states like gels and glasses where dynamic is arrested. This explains why colloidal suspensions are commonly used as model systems to study the dynamical arrest: phase changes can be easily triggered changing parameters like concentration, temperature, pH of the solution, and therefore predictions can be verified through experiments. Biological systems can also be modelled by means of these suspensions, reproducing processes like ageing or self assembly.

Particles suspended in a liquid may form aggregates, because of various kind of attractive intermolecular forces. Particle modifications performed in order to eliminate the attractive interactions that lead to aggregations are called "stabilizations"; this can be done in two different ways, shown in figure 1.2:

- charge stabilization - through the action of a polar solvent an external, electrically-charged layer around the particles is produced, while

Figure 1.1: Gold nanoparticles suspended in water; the radius of the particles determines the colour of the suspension. From [2].

counter-ions floating in the liquid forming an outer layer of opposite charge. Therefore when two such particles approach because coulombian interaction causes repulsion;

- stabilization through entropic forces - when a layer of polymeric chains surrounds particles leading to entropic repulsion, because the layers of different particles can not interpenetrate each other.

In the first case, we have a long-range kind of interaction. Using the second method, instead, we obtain a short-range interaction which reproduces the infinite-wall potential: particles behave as hard spheres.

Silica in water or in glycerol is a well-known example of charge-stabilized system, while PMMA coated with polymers and suspended in decalin, the main sample investigated in this study, is a paradigm of a suspension stabilized by entropic forces.

As concentration increases, attractive forces rise leading to the formation of a gel: this usually happens when the volume fraction is greater then $50 - 60\%$. This process can be called "flocculation", "aggregation", "gelation", and it can occur if the sample is not kept with care, e.g. if the container is left open during a measurement, the solvent evaporates destroying the temporal invariance.
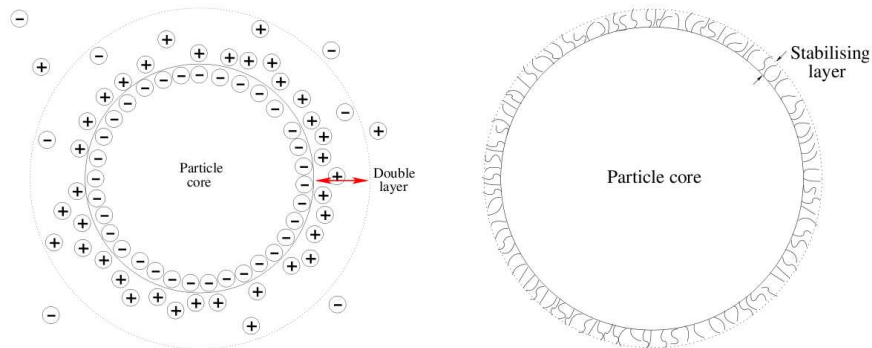
Figure 1.2: Stabilization of colloidal particles. Left: charge stabilization; Right: steric stabilization. From [3].

1.1 Microfluidics applied to X-rays studies

The terms "microfluidics" refers to a group of experimental techniques which involve the use of syringes and tubes (with a radius ranging from $1\mu m$ up to $1mm$) to have the sample flow during a measurement, sometimes mixing the various sample's components in the tube, right before the measurement. There are several reasons, in soft-condensed matter studies, for having the sample flowing in a tube instead of keeping it contained in a capillary or in another container:

- avoid spurious effect given by cavitation and other unwanted modifications in the system's properties induced by the strong x-ray beam, continuously providing new sample; just a syringe and a tube are needed.

- easily measure a time-dependent process like gelation, chemical reactions, phase transitions with a simple experimental setup; using a syringe for every component and T connections, it is possible to mix the sample at the beginning of the tube defining this instant as "$t_0 = 0s$", thus the distance between the mixing point and the beam position is directly linked to time t_1;
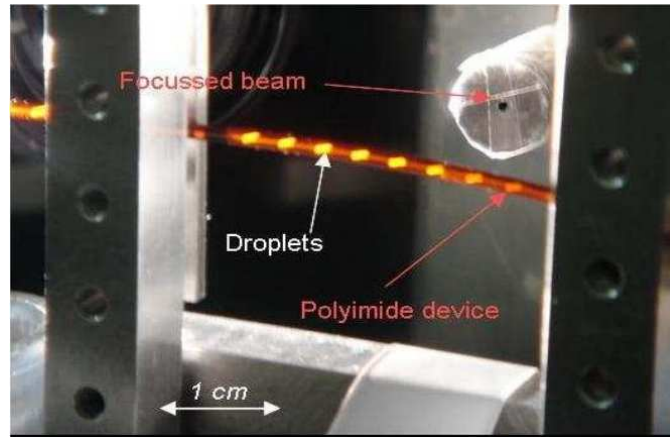
Figure 1.3: Microfluidic device: droplets of sample flowing in an oil stream. Courtesy of Andrei Fluerasu.

- measure sample properties in confined volumes, creating droplets (i.e colloidal suspensions in water, figure 1.3) in a flowing medium (i.e oil); in order to realize this setup at least two syringes are needed, one for the oil and one for the sample, and also a tube-in-tube configuration with tubes with different radius.

All these different kinds of result can be achieved using equipment like tubes, syringes and connections, that are cheap and easy to purchase. However, an important point to be discussed is up to which extent the presence of the flow modifies the intrinsic dynamics of the particles studied. The present thesis work addresses this point. The answer obtained is quite simple: under reasonable conditions, the presence of the flow does not influence the dynamical properties observed, if exchanged momentum $\vec{Q}$ is taken perpendicular to the direction of the flow. This clearly helps the practical realization of the experiment.

Chapter 2

Theoretical framework

2.1 Static structural properties: SAXS

Small Angle X-ray Spectroscopy (SAXS), the measurement of scattered intensity as a function of exchanged momentum $\vec{Q}$, allows the characterization of the structure of interacting colloid systems. Performing SAXS on a low concentration solution of particles gives information about their shape and their size: these quantities can also be measured in high concentration samples, looking at a Q range not too close to zero, for example in the $QR \geq 7$ region. In the very-low-Q range the effects of interaction among particles play a huge role in giving the scattered intensity. The structure of an isotropic system, a colloidal suspension in our case, depends on the size distribution and concentration of the particles, and is usually described by the so-called static structure function $S(\vec{Q})$. This function can be theoretically determined by choosing a model potential to describe the interaction among particles, and by choosing a suitable distribution function for particle's diameter: the resulting expression can be used to fit experimental data.

2.1.1 Scattering theory

The theory of light scattering is based on the following assumptions: first, the intensity of X-ray scattered by the density fluctuations within the medium

can be neglected; second, we consider only single scattering in the first Born approximation, a perturbative method which consist in considering, in each point of the scatterer, only the incident electric field instead of the total electric field also made of the field scattered by other regions of the same object; third, both the particles and the medium are orientationally symmetrical. In this approximation, as reported in [9], the field's amplitude of the X rays scattered by one particle is proportional to

$$b_i(Q) = 4pi \int_0^\infty r^2[\rho(r) - \rho_m]\frac{\sin Qr}{Qr}dr \qquad (2.1)$$

where ρ and ρ_m are the electron densities of the particles and of the medium respectively.

Considering an ensemble of N particles, the total instantaneous amplitude of the scattered electric field at the detector is given by

$$E(Q,t) = K \sum_{i=1}^{N} b_i(Q) \exp[i\vec{Q} \cdot \vec{r}_i(t)] \qquad (2.2)$$

where $\vec{r}_i(t)$ is the position of particle i at time t and K is a constant. Since the intensity is proportional to the square modulus of the amplitude of the electric field, the expression for its ensemble average is just

$$\langle I(Q) \rangle = K^2 \sum_{i=1}^{N} \sum_{j=1}^{N} \left\langle b_i(Q)b_j(Q) \exp[i\vec{Q} \cdot (\vec{r}_i - \vec{r}_j)] \right\rangle \qquad (2.3)$$

Monodisperse particles

For monodisperse particles, $b_i(Q) = b_j(Q)$: in this situation we can easily rewrite last equation in a shorter form:

$$\langle I(Q) \rangle = NK^2 (b(0))^2 P(Q)S(Q). \qquad (2.4)$$

P(Q) is the single particle form factor, and it consists only in a conventional and normalized rewrite of $b(Q)^2$, while S(Q) is the so-called structure factor;

they are given by the following expressions:

$$P(Q) = \left[\frac{b(Q)}{b(0)}\right]^2$$

$$S(Q) = \frac{1}{N}\sum_{i=1}^{N}\sum_{j=1}^{N}\left\langle\exp[i\vec{Q}\cdot(\vec{r}_i - \vec{r}_j)]\right\rangle.$$

In a dilute suspension of colloids, in which we have no correlation between the positions of the particles, S(Q)=1: a SAXS scan provides the form factor of the single particle. Therefore, we can measure $I(Q)$ for a concentrated suspension, and dividing it by the dilute data we obtain a measure of the structure factor $S(Q)$ for this sample. An analytical expression for P(Q) can be obtained resolving the integral in equation (2.1): this calculation gives, as reported in [10],

$$P_{\text{mono}}(Q, R) = \frac{9}{(QR)^6}\left(\sin QR - QR\cos QR\right)^2. \qquad (2.5)$$

This function is characterized by an oscillating profile with minimums in fixed positions: $QR = 4.493,\ 7.725\ldots$. The eventual presence of polydispersity results in a smoother curve, and in different positions for these minimums.

Let's consider the scattering cross section for X-rays: it is given by

$$\frac{\partial\sigma}{\partial\Omega} = \frac{I(Q)}{I_i/A\ \epsilon\ T\ \Delta\Omega} \qquad (2.6)$$

where $I(Q)$ is the scattered intensity, I_i is the incident intensity, A is the beam size, ϵ the detector's efficiency and T the transmission coefficient, namely the ratio between the transmitted and the incident intensities. The transmission coefficient can be obtained through a measurement of the monitor counting, that can be related to the flux of incident photons by a simple calculation which involves some experimental parameters concerning the monitor detector itself. $\Delta\Omega$ is the solid angle seen by a single pixel, which is given by $\Delta\Omega = \frac{d_{pix}^2}{L^2}$: here d_{pix} is the pixel size, L the sample-detector distance.

The form factor P(Q) is related to the differential cross section by the following relation

$$\frac{\partial\sigma}{\partial\Omega} = r_e^2 N P(Q) S(Q). \qquad (2.7)$$

which is a mere manipulation of equation (2.4), and is reported in [11]. In this equation, r_e^2 is the classical electron radius and N the number of particles, which is related to the volume fraction Φ of the sample: $\Phi = \frac{N V_{part}}{V_{sample}}$. In this case, V_{part} is the volume of a single silica sphere, while V_{sample} is the scattering volume, namely the product between the beam size A and the mean width l of the water droplet.

Using equations (2.6) and (2.7), deriving an expression for the volume fraction of the sample is possible:

$$\Phi = \left(\frac{I(Q)}{P(Q)} \right) \frac{V_{part}}{r_e^2 \ I_i \ l \ \epsilon \ T \ \Delta\Omega} \tag{2.8}$$

The scale parameter $\frac{I(Q)}{P(Q)}$ can be obtained through fitting: by means of this simple calculation, we can easily measure the concentration of a sample.

Polydisperse particles

Now we can complicate a little bit the situation, considering a distribution of sizes that makes $b_i(Q)$ vary from particle to particle as a consequence of different sizes and shapes of the particles. An analytical solution of equation (2.3) can be found only in few cases: one of whom will be shown in the following paragraph. Instead an approximated, but applicable to many situations, approach is possible.

As in [12], we made the assumption that particle size and orientation are uncorrelated with the position of the particles. Then we can rewrite equation (2.3) by averaging the term $b_i(Q)b_j(Q)$ with a weight given by the distribution of particle sizes and orientation:

$$\langle I(Q) \rangle = \sum_{i=1}^{N} \sum_{j=1}^{N} \langle b_i(Q)b_j(Q) \rangle \left\langle \exp[i\vec{Q} \cdot (\vec{r}_i - \vec{r}_j)] \right\rangle \tag{2.9}$$

$$\langle b_i(Q)b_j(Q) \rangle = \begin{cases} \overline{b^2(Q)} & \text{if } i = j \\ \overline{b(Q)}^2 & \text{if } i \neq j \end{cases}$$

We can write a more understandable form of this equation, that uses some notation we reported for monodisperse particles.

$$\langle I(Q) \rangle = N \left(b(0) \right)^2 P(Q) \left\{ 1 + \beta(Q) \left[S(Q) - 1 \right] \right\}. \qquad (2.10)$$

$$\beta(Q) = \frac{\overline{b(Q)}^2}{\overline{b^2(Q)}} \quad P(Q) = \frac{\overline{b^2(Q)}}{[b(0)]^2}$$

$$S(Q) = \frac{1}{N} \sum_{i=1}^{N} \sum_{j=1}^{N} \left\langle \exp[i\vec{Q} \cdot (\vec{r}_i - \vec{r}_j)] \right\rangle.$$

2.1.2 Polydisperse hard spheres

Most of the samples studied in this work are well described by an hard spheres model, in which their polydispersity is taken into account. The interactions among particles, important if volume fraction is higher than $5 - 6\%$, are of the "excluded volume" kind, and they lead to a structure factor different from 1. Analytical expression for the structure factor can be obtained by applying the Percus-Yevich approximation to the Hamiltonian of this system.

In order to obtain an analytical expression of the form factor for spherical particles, it is useful to switch to integrals instead of summations in the calculation of $P(Q)$, the polydisperse form factor, and of $\beta(Q)$, a factor between zero and one that suppress the oscillations of the structure factor in the observed scattering intensity. Both involves the scattered amplitude $b_i(Q)$, as they contains the square power of its average and the average of its square power.

$$\overline{b(Q)}^2 = \left| \int_0^\infty \sqrt{P_{\text{mono}}(Q, R)} \, f(R) \, dR \right|^2 \qquad (2.11)$$

$$\overline{b^2(Q)} = \int_0^\infty P_{\text{mono}}(Q, R) \, f(R) \, dR \qquad (2.12)$$

Here $f(R)$ is the particle size distribution centered at $R = \overline{R}$, where $\overline{R}$ is the mean radius. Usually the gamma (Schulz) distribution is chosen, for its mathematical tractability. This distribution tends to the Gaussian one as

its width parameter, Z, tends to infinity; the polydispersity of the sample is given by $\sqrt{\frac{1}{Z+1}}$ (Z is always major than -1) while the standard deviation of the radius of the particles is given by $\sigma = \frac{\overline{R}}{\sqrt{Z+1}}$.

$$f(R) = \left(\frac{Z+1}{\overline{R}}\right)^{Z+1} R^Z \exp\left[-\left(\frac{Z+1}{\overline{R}}\right) R\right]/\Gamma(Z+1) \qquad (2.13)$$

An analytical solution of integrals (2.11) and (2.12) for gamma-distributed sizes is reported in [12]. Thus, now we have an analytical expression for both $P(Q)$ and $\beta(Q)$: an example is shown in figure 2.1.
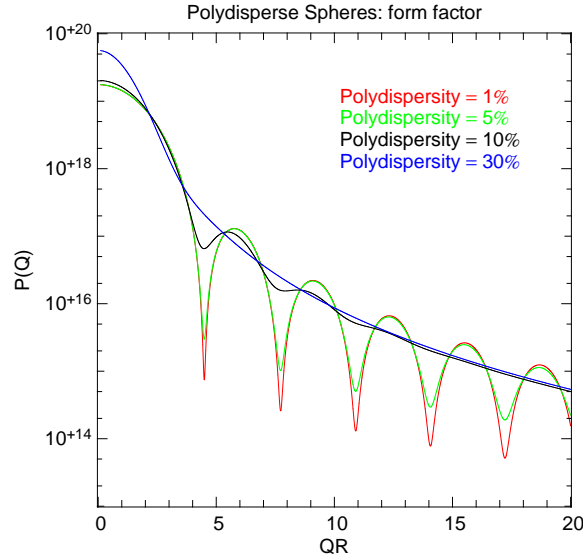

Figure 2.1: Form factors of hard spheres, with different polydispersity

An analytical expression for the structure factor is derived in [4] for spheres with excluded-volume interactions and Schulz distributed size: an example of what we obtain is reported in figure 2.2, which is an exact reproduction of a figure in the article cited before. The $S(Q)$ expression is quite lenghty but simple to understand: the mean in equation (2.1.1) is performed as an integral from 0 to ∞, that can be easily solved due to the properties of the Shulz-Gamma distribution:

$$S(Q) = 1. - \frac{2ph}{x^3(X^2 + Y^2)} \qquad (2.14)$$

$$h = \lambda[\lambda(Y\delta_1 - X\delta_6) + \lambda'(Y\delta_2 - X\delta_4) + \mu(X\delta_1 + Y\delta_6) + \mu'(X\delta_2 + Y\delta_4)]$$
$$+\lambda'[\lambda(Y\delta_2 - X\delta_4) + \lambda'(Y\delta_3 - X\delta_5) + \mu(X\delta_2 + Y\delta_4) + \mu'(X\delta_3 + Y\delta_5)]$$
$$+\mu[\lambda(X\delta_1 + Y\delta_6) + \lambda'(X\delta_2 + Y\delta_4) + \mu(X\delta_6 - Y\delta_1) + \mu'(X\delta_4 - Y\delta_2)]$$
$$+\mu'[\lambda(X\delta_2 + Y\delta_4) + \lambda'(X\delta_3 + Y\delta_5) + \mu(X\delta_4 - Y\delta_2) + \mu'(X\delta_5 - Y\delta_3)]$$

$$X = 1 - (2\pi/\Delta)(1 + \tfrac{1}{2\Delta}\pi\eta_3/)(\rho Q^{-3})(Q\zeta_1 - \psi_0)$$
$$- (2\pi/\Delta)(\rho Q^{-2})[(\chi_1 - \zeta_1) + \tfrac{1}{4\Delta}\pi\eta_2/(\chi_2 - \zeta_2)]$$
$$- (\pi/\Delta)^2(\rho Q^{-2})^2[(\chi_0 - 1)(\chi_2 - \zeta_2) - (\chi_1 - \zeta_1)^2 - (Q\zeta_1 - \psi_0)(Q\zeta_3 - \psi_2) + (Q\zeta_2 - \psi_1)^2]$$

$$Y = (2\pi/\Delta)(1 + \tfrac{1}{2\Delta}\pi\eta_3/)(\rho Q^{-3})(\chi_0 + \tfrac{1}{2}Q^2\zeta_2 - 1)$$
$$- (2\pi/\Delta)(\rho Q^{-2})[(Q\zeta_2 - \psi_1) + \tfrac{1}{4\Delta}\pi\eta_2/(Q\zeta_3 - \psi_2)]$$
$$- (\pi/\Delta)^2(\rho Q^{-2})^2[(Q\zeta_1 - \psi_0)(\chi_2 - \zeta_2) - 2(Q\zeta_2 - \psi_1)(\chi_1 - \zeta_1) + (Q\zeta_3 - \psi_2)(\chi_0 - 1)]$$

$$(2.15)$$

$$b = 2R/(Z+1) \qquad c = (Z+1)$$

$$\overline{R^3} = (Z+2.)(Z+3)R^3/(Z+1)^2 \qquad \rho = \Phi/(\tfrac{4}{3}\pi\overline{R3})$$

$$\eta_1 = \rho bc \qquad \eta_2 = \rho b^2 c(c+1) \qquad \eta_3 = \rho(b^3 c(c+1)(c+2))$$

$$\Delta = 1 - \pi\eta_3/6 \qquad \nu_1 = 1/(1+(bQ)^2) \qquad \nu_2 = 1/(4+(bQ)^2)$$

$$\zeta_1 = bc \qquad \zeta_2 = b^2 c(c+1) \qquad \zeta_3 = b^3 c(c+1)(c+2)$$

$$\psi_0 = \nu_1^{c/2} \sin[c\tan^{-1}(bQ)]$$
$$\psi_1 = bc\nu_1^{(c+1)/2} \sin[(c+1)\tan^{-1}(bQ)]$$
$$\psi_2 = b^2 c(c+1)\nu_1^{(c+2)/2} \sin[(c+2)atan(bQ)]$$

$$\mu = 2^c \nu_2^{c/2} \sin[c\tan^{-1}(bQ/2)]$$
$$\mu' = 2^{c+1} bc\nu_2^{(c+1)/2} \sin[(c+1)\tan^{-1}(bQ/2)]$$

$$\chi_0 = \nu_1^{c/2} \cos[c\tan^{-1}(bQ)]$$
$$\chi_1 = bc\nu_1^{(c+1)/2} \cos[(c+1)\tan^{-1}(bQ)]$$
$$\chi_2 = b^2 c(c+1)\nu_1^{(c+2)/2} \cos[(c+2)\tan^{-1}(bQ)]$$

$$\lambda = 2^c \nu_2^{c/2} \cos[c\tan^{-1}(bQ/2)]$$
$$\lambda' = 2^{c+1} bc\nu_2^{(c+1)/2} \cos[(c+1)\tan^{-1}(bQ/2)]$$

$$\delta_1 = (\pi/\Delta)(2 + (\pi/\Delta)(\eta_3 - (\rho/Q)(Q\zeta_3 - \psi_2)))$$
$$\delta_2 = (\pi/\Delta)^2(\rho/Q)(Q\zeta_2 - \psi_1)$$
$$\delta_3 = -(\pi/\Delta)^2(\rho/Q)(Q\zeta_1 - \psi_0)$$
$$\delta_4 = (\pi/\Delta)(Q - (\pi/\Delta)(\rho/Q)(\chi_1 - \zeta_1))$$
$$\delta_5 = (\pi/\Delta)^2((\rho/Q)(\chi_0 - 1) + \tfrac{1}{2}Q\eta_2)$$
$$\delta_6 = (\pi/\Delta)^2(\rho/Q)(\chi_2 - \zeta_2)$$

$$(2.16)$$

Using these equations we can now fit experimental data and obtain a measure of the mean radius of the particles, of their polydispersity and of their concentration.
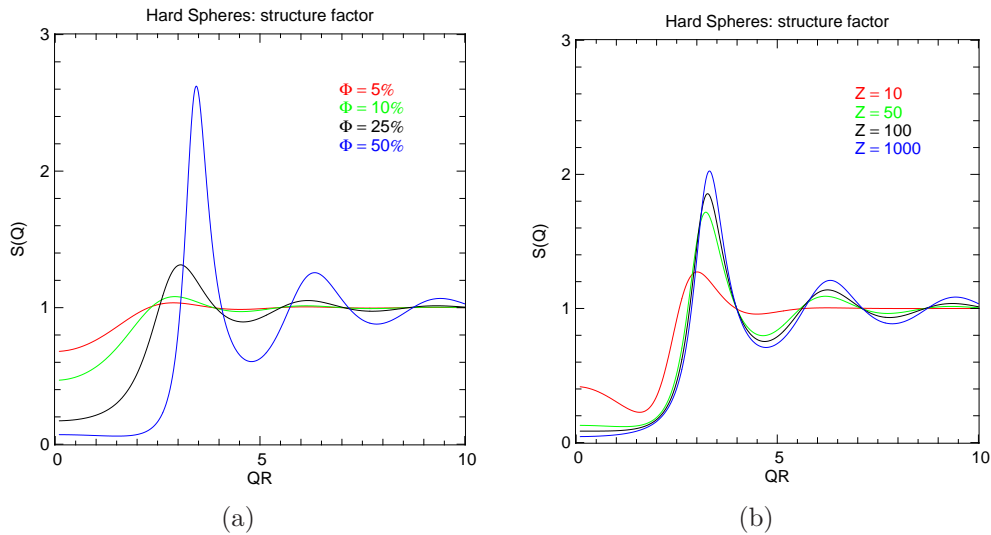

Figure 2.2: a)Structure factors of hard spheres, with fixed polydispersity, at different concentrations; b)Structure factors of hard spheres, with concentration fixed at 40%, at different values of polydispersity.

Another model for the intensity as a function of Q is reported in [4]. It is an analytical solution of equation (2.3) for a Schulz-polydisperse hard spheres fluid, in the Percus-Yevich approximation. The differences between this last formula and $P(Q) \cdot S(Q)$ is shown in figure 2.3.

Core-shell model: comparison

In order to achieve better results, another model for the form factor was considered: the core-shell particle model. Since our sample consists of stearic stabilized particles, taking into account the contribution to the scattering of the polymeric layer around the particle may lead to better results in fitting the experimental results. An analytical solution was obtained in [13]; this expression has more parameters than the hard-sphere model: the particle's
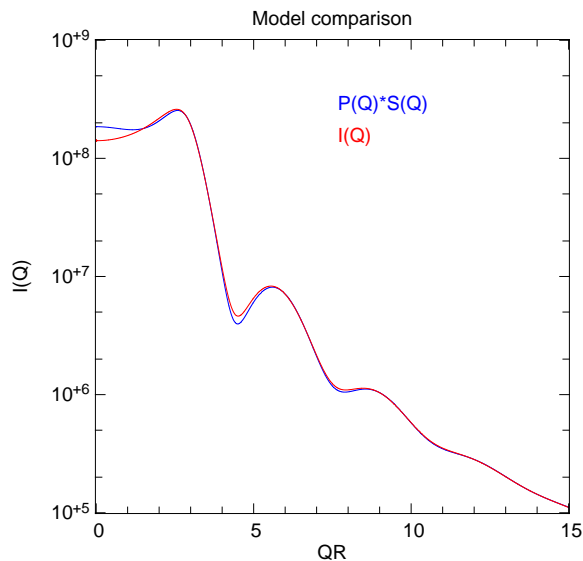
Figure 2.3: Comparison between the analytical solution of equation (2.3) and the approximation $P(Q) \cdot S(Q)$

radius, the shell thickness, the electron densities of the core, the shell and the medium, the size's polydispersity and the concentration. Of course, this model must lead to the same results of the hard sphere one in case the shell as null thickness, or it is made of the same material of the core: this is shown in figure 2.4

The increasing number of particles allows, obviously, to describe a greater number of samples: in our case, with a shell thickness of the order of 1% of the total radius, we see no improvements at all respect to the hard sphere model. Therefore, the "core-shell particles" model was not used during data analysis.

2.2 Dynamics: XPCS

In this chapter, having illustrated what can be measured through a SAXS experiment, we want to show how the dynamics of our sample can be studied by XPCS, X-ray Photon Correlation Spectroscopy. Photon Correlation Spectroscopy is a technique that usually involves visible light; although, there are
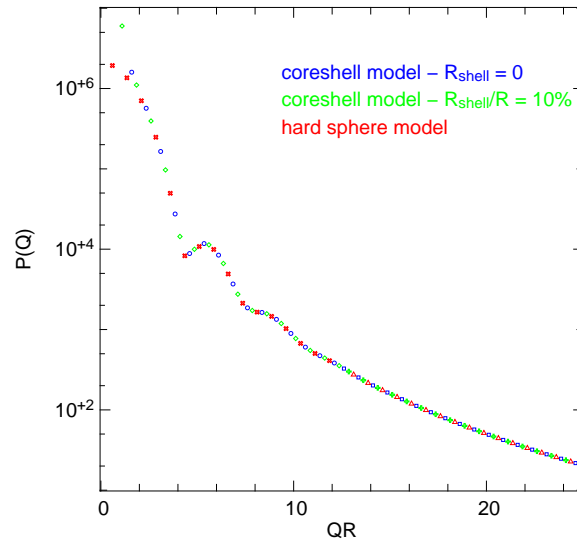
Figure 2.4: Comparing the hard sphere and the core-shell particle models: the red curve is the result for the hard-sphere model, the blue one is given by the core-shell model with shell not present, the red one represents a core-shell model with a shell made of the same material of the core.

several advantages in using X-rays instead:

- it is possible to study matter on the inter-atomic length scale, since it is possible to reach high values of the exchanged momentum Q;

- it is possible to study optically opaque samples, since multiple scattering, one of the main difficulties in light scattering, is negligible.

These results can be achieved as well using Neutron Scattering, but by means of X-rays only a relatively small quantity of sample is required, while the high flux of photons, compared to the much lower neutron flux, allow fast data detections. On the other hand, several advantages connected to the use of neutrons are lost, like the ones introduced by deuteration or other techniques very useful in soft-matter studies.

2.2.1 Coherent X-rays

Visible light coherence is obviously obtained using a laser source. It is possible also to use an incoherent source like an X-ray undulator, with an high collimated and monochromatic beam, to obtain coherent light: in this case the intensity of coherent light is directly proportional to the brilliance of the source. Since third generation synchrotrons produce coherent X-rays several order of magnitudes more intense than in the past, this kind of studies are now possible: with the enormously higher amount of photons there are no problems in losing many of them by collimation in order to obtain a high-coherence beam. Coherence is the correlation between the phase of a light wave at different points or instants, separated by a certain distance or a certain delay. Transverse (d) and longitudinal (l_{coh}) coherence length can be defined as the distances at which the wave still holds a specified degree of coherence: they are related to the wavelength and other experimental parameters by means of simple expressions:

$$l_{coh} = \frac{\lambda^2}{2\delta\lambda}$$

$$l_t = \frac{\lambda R_s}{2d_s}$$

where λ is the wavelength, $\delta\lambda$ the standard deviation of its distribution, R_s the distance from the source and d_s is the source size. Using a pinhole of size comparable to the coherence length result in a coherent beam. At ID10A, a flux major than $10^9 \frac{ph}{sec \cdot 100mA}$ of monochromatic x-rays ($\frac{\Delta E}{E} = 1.4 \cdot 10^{-4}$) is obtained using a 10x10 μm^2 pinhole.

A demonstration that synchrotron radiation is characterized by sufficient coherence, despite being generated by an incoherent source, is the measurement of Fraunhofer diffraction pattern of a pinhole, as reported in figure 2.5.
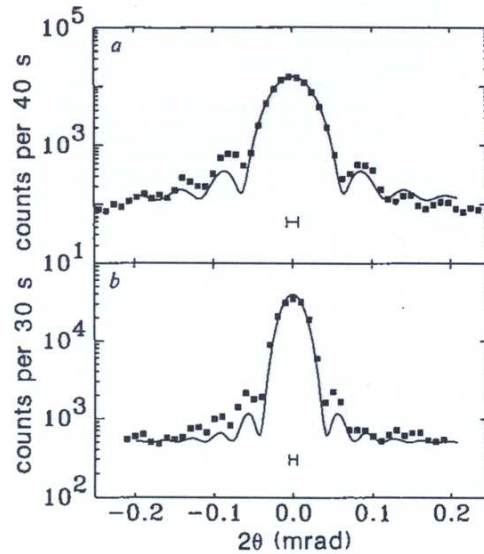
Figure 2.5: Fraunhofer diffraction from a, $2.5\mu m$ and b, $5\mu m$ diameter pin-holes [14]

2.2.2 Speckles and correlation functions

Coherent radiation scattered from a disordered sample results in a random diffraction or "speckle" pattern, which is due to interference of many waves with different phases. The use of incoherent light would lead to an averaged pattern, whit consequent loss of information. Since it is due to the disorder, it is possible to access the dynamics of the sample study of speckle's changes with time .

Although speckles obtained with visible light are well known, X-rays speckle patterns have been observed for the first time in 1991 [14], measuring the diffuse (001 crystallographic direction) peak from an ordered single crystal of Cu_3Au. Such a crystal was made of a random arrangement of domains given by the four different ways in which the single unit can occupy a lattice's site.

It is not a immediate task to perform an XPCS experiment; indeed, there are some general conditions necessary to be satisfied, provided by [15]:

- the scattering volume size must be comparable with the coherence volume one, given by the product of the coherence lenghts;

- the scattering should be broad enough, thus the sample should be enough disordered on the spatial scale of the scattering volume;

- a sufficiently high number of counts per correlation time must be provided;

- a good statistic is needed, provided by a sufficient number of correlation times - a good number of points into the correlation function - thus by an adequate number of speckles.
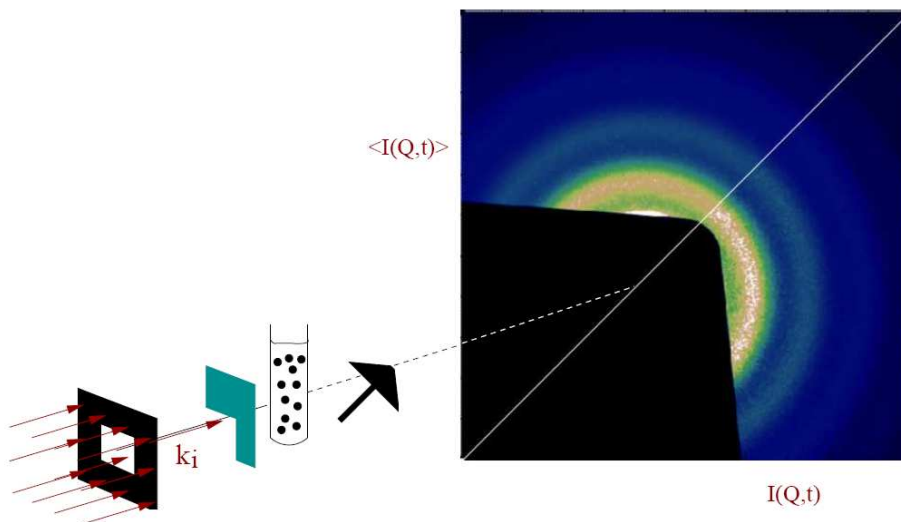

Figure 2.6: Speckle pattern. On the left-upper side of the 2d image, a radial average of the pattern was performed. Courtesy of Andrei Fluerasu

The speckle pattern reflects the disorder of the sample contained in the scattering volume. The study of the speckle pattern's changes provide information regarding the motion of the particles. This leads to a well known visible-light technique, called either Intensity Fluctuation Spectroscopy (IFS), Dynamic Light Scattering (DLS) or Photon Correlation Spectroscopy (PCS). A first variable quantity we can look at is the first-order correlation function,

related both to the electric field of the light we are measuring and to the first-order coherence of light:

$$g^{(1)}(\tau) = \frac{\langle E^*(t)E(t+\tau)\rangle}{\langle E^*(t)E(t)\rangle} \tag{2.17}$$

We can also deal with the so-called second-order coherence of light through the normalized correlation function of intensity, thus directly related to what we really measure during a scattering experiment:

$$g^{(2)}(\tau) = \frac{\langle I^*(t)I(t+\tau)\rangle}{\langle I^{(t)}\rangle^2} \tag{2.18}$$

It is possible to demonstrate that using Gaussian distributed light those quantities are connected by a very simple relation:

$$g^{(2)}(\tau) = 1 + \left|g^{(1)}(\tau)\right|^2 \tag{2.19}$$

Since $g^{(1)}(\tau)$ is equal to the normalized intermediate scattering function, we can provide a simple model for $g^{(2)}(\tau)$; we have that

$$g^{(1)}(\tau) = \frac{F(\vec{Q},t)}{F(\vec{Q},0)} \tag{2.20}$$

Here $F(\vec{Q},0)$ can be identified with the static structure factor while $F(\vec{Q},t)$, the intermediate scattering function or dynamic structure factor, is given by

$$F(\vec{Q},t) = \frac{1}{Nf^2(\vec{Q})}\sum_n\sum_m\left\langle f_n(\vec{Q})f_m(\vec{Q})e^{i\vec{Q}[\vec{r}_n(0)-\vec{r}_m(t)]}\right\rangle \tag{2.21}$$

where the brackets indicate an ensemble average over the scattering amplitudes $f_n(\vec{Q})$.

A simple example is given by a low-concentration colloidal suspension of monodisperse spherical particles under Brownian motion. In this situation the mean square value for particle displacement is $6D_0t$, proportional to the diffusion coefficient

$$D_0 = \frac{k_BT}{6\pi\eta R} \tag{2.22}$$

The intermediate scattering function is just the Fourier transform of the space-time correlation function G which gives the probability that, having a

particle in a certain position at time t, there is another particle at distance $\vec{r}$; for Brownian motion, this function is a Gaussian curve:

$$G(\vec{r}, t) = (4\pi D_0 t)^{-\frac{3}{2}} \exp\left[-\frac{r^2}{4D_0 t}\right]. \tag{2.23}$$

The Fourier transform of a Gaussian curve is another Gaussian curve in the reciprocal space:

$$F(\vec{Q}, t) = \exp\left[-DQ^2 t\right]. \tag{2.24}$$

The second-order correlation function is then equal to

$$g^{(2)}(\tau) = 1 + \left|\frac{F(\vec{Q}, t)}{F(\vec{Q}, 0)}\right|^2 = 1 + e^{-2D_0 Q^2 t}. \tag{2.25}$$

This expression is not valid anymore when inter-particle interaction are present. Keeping the exponential form of the correlation function is still possible, simply introducing a wavevector-dependent diffusion coefficient D(Q). The effects of interactions are therefore included in the time constant only, which is not constant over Q anymore. Moreover, this technique is valuable while studying very interesting out-of-equilibrium samples in which dynamic properties change in time, the sample undergoing a process of aging were the temporal invariance is broken. Correlation functions are now characterized by a diffusion time which is a function of time, as well as of Q. Informations about these processes can be retrieved from the speckle pattern through the so-called two-times correlation function, as first proposed in [16]:

$$Corr(Q, \tau_1, \tau_2) = \frac{\langle I(Q, \tau_1) I(Q, \tau_2)\rangle}{\langle I(Q, \tau_1)\rangle \langle I(Q, \tau_2)\rangle}. \tag{2.26}$$

The function has its maximum on the diagonal: going away from it, the function decays to one. If contour lines are parallel to the diagonal, then the sample does not ages.

Chapter 3

Experimental details

3.1   SAXS and XPCS at ID10A, ESRF

ID10A is a multipurpose, high-brilliance undulator beamline at ESRF, the European Synchrotron Radiation Facility. Composed by two different experimental hutch, it provides either XPCS, high resolution X-ray scattering (XD), coherent SAXS or biological Coherent Diffraction Imaging (CDI); it is dedicated to the study of structural and dynamic properties of soft and hard condensed matter. This thesis work has been carried out there, measuring both static properties and correlation functions. Technical informations about ID10A are reported in its website [17].

The X-ray source consists of three undulator: one 27 mm undulator (U27), one 35 mm undulator (U35), and a revolver unit carrying both U27 and U35 undulators. Therefore, undulators total scheme can be changed depending on energy requirements. The source size, in other words the Full Width at Half Maximum (FWHM) of the profile of the beam, is equal to $928\mu m$ in the horizontal direction and to $23\mu m$ in the vertical one. Typical divergences at 10 keV, still intended in terms of FWHM, are $28\mu m$ in horizontal direction and $17\mu m$ in vertical, implying a maximum beam size of respectively 2 mm and 0.8 mm at the TROIKA I monochromator position, located 44.2 m away from source. The monochromaticity of the beam

is assured by a multi-crystal single bounce monochromator that consists of three different monochromator crystals: diamond(111), diamond(220), and silicon(111). Beryllium compound refractive lenses (CRL) or a double mirror system can be used to focus the beam, which is reduced by a system of slits to a size of $10x10\mu m^2$ at sample position.

3.1.1 Detectors

ID10A's experimental hutch is equipped with both point detectors and 2D detectors, operating at different frequencies. Normally a 2D detector is preferred, since it allows measurements of correlation functions at different $\overrightarrow{Q}$ during the same measurement. The main limitation of this kind of detectors is the low frame-rate, which does not allow fast dynamics measurements; this problem is partially solved by the new MEDIPIX-II detector. Anyway, the dynamics of some samples can be studied only by means of a fast point detector.

Figure 3.1: BICRON scintillator counter, ID10A, ESRF.

Point detector

ID10A's point detector is a BICRON scintillator counter, model 1XM.040B - PMT type R580, with beryllium entrance window. Its circular crystal has

a radius of $2.54cm$ and a $1mm$ thickness, while its energy range from 3 up to 100 keV; its count rate ranges up to $30000cts/sec$. The point detector is commonly used during the alignment procedures as well, and also in addition to a 2D detector to measure the intensity of the transmitted beam through the sample under study, so that the total attenuation can be deduced.

2D detectors

There are two two-dimensional detectors available at ID10A, with different frame-rates and detection areas. Each has to be equipped with a beam-stop to avoid detection of the direct beam, which will obviously cause damage to the sensitive area. The first 2D detector is an high resolution water-cooled CCD camera, from Princeton Instruments, consisting of 1152x1242, $22.5\mu m$ pixel. The very long reading time ($\simeq 1s$) between two different frames is the main problem of this detector. This time can be reduced selecting a smaller active area, but still detecting fast dynamics is impossible. Subtracting a measurement done with no beam is mandatory in order to obtain useful data: the degradation of the chip under direct illumination by hard X-rays is inevitable, even when it is used to detect weak signals in photon-counting mode (less than $100\frac{ph}{pix\cdot s}$), leading to the presence of dead pixels and "ghost" images.

The second detector is a 2D array of CMOS pixel cells working in single-photon-counting. A threshold can be tuned to measure every single photon hitting the active area, thus avoiding the need of "dark" measurement. Since the reading time is almost equal to $60\mu s$, we can acquire up to 1000 images per second, with 16000 images as maximum. Therefore, the study of dynamics characterized by a time-scale of the order of the hundredth of a second is made possible using this detector. Waiting time option and a synchronized shutter are also disposable, to allow long measurements avoiding beam damage.

Figure 3.2: Medipix 2 detector: the area behind the aluminum strip can contains up to 5 sensors.

3.1.2 Multi-tau correlator

The calculation of the intensity-intensity correlation functions is carried out by a software program, when we are using a 2D detector, or by an electronic device, if we are using a point detector; both are called "correlators". It is meaningless trying to calculate a correlation function by a "brute force" approach, using the mathematical definition of $g^2(\tau)$ given by equation (2.18): it will require an enormous amount of time and of computational resources to perform an average, given a correlation time τ, over every couple of values of the intensity separated by that time. A different approach is needed: the multi-tau correlator, which can be implemented both as a software and as an electronic device. A multi-tau correlator is a combination of many "usual" correlators, each of them working, at the same time, only using one correlation time τ [18] [19]. Each correlator works using a correlation time τ which is doubled respect to the time used by the previous correlator. This way, the correlation function can be computed during data acquisition: since

the calculation starts from small correlation times, we have many couples of intensity values to average even is the measurement has just begun.

Figure 3.3: Hardware Correlator Flex01-08D, with two input connections and an USB output.

The point detector is equipped with a multi-tau hardware correlator, Flex01-08D from correlator.com, equipped with 1088 real time channels and with a minimum correlation time of $8ns$. Correlation functions from 2D detector's data are calculated using software multi-tau correlators, available in many languages like Matlab, Python, Yorick.

3.2 Statistical analysis in PCS

In order to study the dynamical properties of a sample by XPCS, we must find a way to estimate the statistical error of correlation functions calculated through a multi-tau algorithm. An expression for the variance of the correlation function must be found, keeping in mind that the standard deviation is the square root of the variance.

We are not dealing with a simple calculation, since it involves the variance of summations and products of correlated random variables, namely the intensities measured at each frame; ordinary statistics books usually report expressions for uncorrelated random variables.

3.2.1 Low count rate limit

In this section the theory developed in [20] is reported, just with some changes in the notation.

We can start evaluating the error of the unnormalized correlation function

$$\widehat{G}^{(2)}(\tau) = \frac{1}{M} \sum_{i=1}^{M} n(t_i + \tau) n(t_i)$$

of the intensities detected during an experimental time T: it can be expressed as

$$var\left(\widehat{G}^{(2)}(\tau)\right) = \frac{var(n(\tau)n(0))}{M} + \frac{2}{M} \sum_{k=1}^{M-1} \left(1 - \frac{k}{M}\right) \times$$
$$\times \left[\langle n(k\tau_a + \tau)n(k\tau_a)n(\tau)n(0)\rangle - \left(\widehat{G}^{(2)}(\tau)\right)\right]. \tag{3.1}$$

Here, $n(t)$ is the measured intensity, or count rate, recorded at time t during the accumulation time τ_a, while M is the number of averaged correlated pairs.

For the moment, it is better to start from a simpler situation, when the averaged number of counts per frame is low:

$$\overline{n} << 1$$

This condition is easily satisfied using a Fast Point Detector characterized by a very short acquisition time. The use of a CCD may cause some problems if the exposure time is too long, a feature needed in order to measure slow dynamics; this will lead to significantly high count rate, specially at low Q. Anyway, using this approximation we can consider, in equation (3.1), only the terms of the lower order in $\overline{n}$. It can be shown that these terms rise only from the first addendum:

$$var\left(n(\tau)n(0)\right) = \langle n(\tau)n(0)\rangle + O(\overline{n}^3) \simeq G^{(2)}(\tau)$$

Then, the approximated expression for the variance of the unnormalized correlation function is

$$var\left(G^{(2)}(\tau)\right) \simeq \frac{G^{(2)}(\tau)}{M}. \tag{3.2}$$

This is only a first step: the quantity measured during an experiment is the normalized correlation function;

$$\widehat{g}^{(2)}(\tau) = \frac{G^{(2)}(\tau)}{\overline{n}^2} = \frac{M^{-1}\sum_{i=1}^{M} n(t_i + \tau)n(t_i)}{\left[M^{-1}\sum_{i=1}^{M} n(t_i)\right]^2}. \tag{3.3}$$

Strictly speaking, the last equation returns only a biased estimator of the normalized correlation function; the deviation experienced from the ideal value is of the order of the square of the variance of $\widehat{g}^{(2)}(\tau)$, therefore complicating the notation is useless. From now, we are not going to make distinctions between this expression and the real correlation function.

Knowing the variance of the unnormalized correlation function, deriving the expression of the variance of the normalized one, although as an approximation, does not require much efforts. If we expand (3.3) to the second order in terms of the deviations from the mean values of n and $G^{(2)}$, we obtain the following expression, which is true if M is sufficiently large:

$$var\left(g^{(2)}\right) = \frac{var\left(G^{(2)}\right)}{\overline{n}^4} + 4\frac{g^{(2)}}{\overline{n}^2}var(n) - \frac{4g^{(2)}}{\overline{n}^3}\left[\langle nG^{(2)}\rangle - \overline{n}^3 g^{(2)}\right] \tag{3.4}$$

Since we are in the limit $\overline{n} << 1$, every term except for the first can be neglected, and therefore we can apply equation (3.2) to obtain a simple and very useful expression:

$$var\left(g^{(2)}(\tau)\right) = \frac{\widehat{g}^{(2)}(\tau)}{M(\tau)\overline{n}^2} \tag{3.5}$$

where M is the number of correlated pair averaged in the calculation of $g^{(2)}(\tau)$, therefore it is a function of τ, while $\overline{n}$ is the mean intensity per frame. In applications, we have to be very careful: the true meaning of expression like "accumulation time" or "per frame", that we have used so far, must be sorted out.

CCD detector

Now we can apply the results obtained to the real case of a CCD detector, expressing $M(\tau)$ in a more understandable form; a similar calculation is reported in [21]. Let's consider the calculation of a correlation function over N frames, each of them with an exposure - or accumulation - time τ_a, collected during a total experiment time T. The number of correlated pair at the minimum delay time $\tau = \tau_a$ is simply $N - 1$: in other words, we have

$$M = \frac{T - \tau}{\tau_a}$$

We could take into account a read-out time τ_r and an optional "sleep" time τ_s, with a total time between consecutive frames $\tau_f = \tau_a + \tau_r + \tau_s$. Moreover, using a CCD means that we are averaging over N_{pix} times more correlated pairs, where N_{pix} is the number of pixels. This lead to the more general expression

$$M = N_{pix}\frac{T - \tau}{\tau_f}.$$

Finally, equation (3.5) for the variance of the correlation function can be rewritten as

$$var\left(g^{(2)}(\tau)\right) = \frac{\tau_f\, g^{(2)}(\tau)}{N_{pix}\,(T - \tau)\,\overline{n}^2}. \tag{3.6}$$

It is worth noting that uncertainty grows as τ approaches the total measurement time T: when the difference $(T - \tau)$ goes to zero, the error bar diverges. This make sense, because at high delay times we are averaging on less and less correlated pairs.

Point detector

Equation (3.6) can be easily adapted to the case of a single-point fast detector coupled with an hardware multi-tau correlator. Such correlator doubles the accumulation time and the delay time every L channels. We can express the accumulation time corresponding to every point of the correlation function as the difference between the delay times of the considered point and of the one next to it. Moreover, we can neglect the read-out time, while the

"sleep" time is not present. Photon counts per second, I, are the output of the hardware correlator. This quantity is related with n by the relation $n = I\tau_a$. Bearing this in mind, the expression of the variance of the correlation function is simply

$$var\left(g^{(2)}(\tau)\right) = \frac{g^{(2)}(\tau)}{(T-\tau)\,\overline{I}^2\tau_a}.$$ (3.7)

Signal-to-noise ratio

A useful parameter of the goodness of a measure is the so-called Signal-to-noise ratio, or SNR. For a correlation function, it is usually defined as

$$SNR = \frac{g^{(2)}(\tau) - 1}{\sqrt{var\left(g^{(2)}(\tau)\right)}}$$ (3.8)

Sometimes a rough estimator of SNR is desirable; in particular, we can make a low contrast approximation for an ideal single point detector. In such a limit we have

$$\begin{cases} g^{(2)}(\tau) \simeq 1 + \beta \\ \sqrt{g^{(2)}(\tau)} \simeq 1 \end{cases}$$

thus we obtain

$$SNR = \beta\,\overline{I}\sqrt{(T-\tau)\tau_a}$$ (3.9)

an expression reported in [22] as well.

3.3   Sample preparation

The main subjects of this research were colloids made of poly(methilmethacrylate) - or PMMA - spheres coated by a thin external layer of poly-12-hydroxystearic acid, suspended in decalin (figure 3.5).

Decalin, or decahydronaphthalene, is an organic industrial solvent. Colorless and with a strong aromatic odor, it is less dense than water having $\rho = 0.896$. It presents two different forms, cis and trans (figure (3.4)): in this work we used a mix of the two because of its lower cost, since a large quantity of sample goes wasted during a flow experiment.
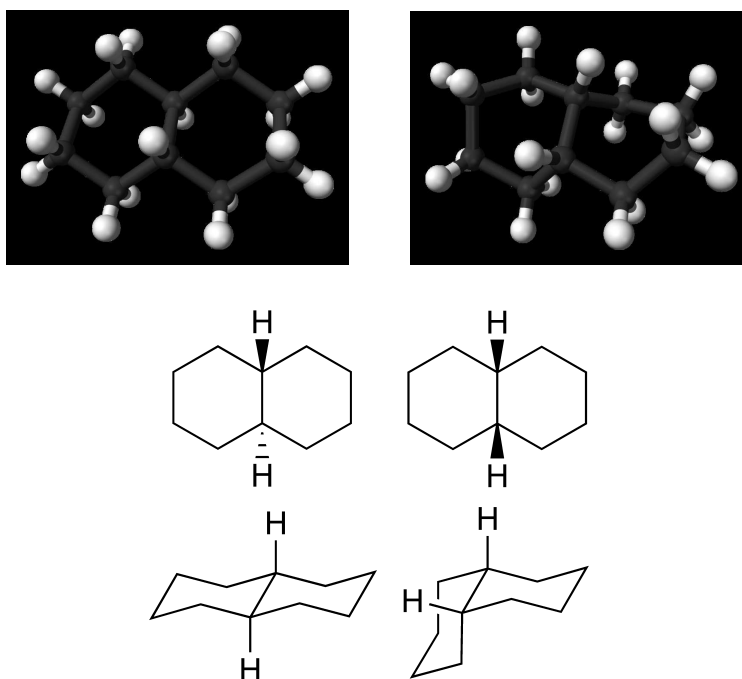
Figure 3.4: Decalin: trans (left) and cis (right) forms.

PMMA colloidal systems were studied for the first time by Pusey and Van Megen [23], showing their hard-sphere behaviour. The total radius of the particles was around $90nm$, with $1nm$ given by the polymeric layer which provides hard-sphere behaviour to the sample through steric stabilization. Particles are electrically neutral, therefore they interact only through entropic forces.

The stock sample had a volume fraction $\Phi = 0.327$. Preparation of diluted samples was initially performed diluting the stock suspension with decalin obtained from centrifugation of the sample itself; decalin is a mix of its trans and cis forms, and a priori the effects of using another mixture of decalin, with different percentages of cis and trans isomers, are unknown. This led to various problems, mainly due to the altered distribution of radius respect to the one of the original sample: the decalin obtained from centrifugation can contain small or broken particles. Therefore, dilution with new decalin
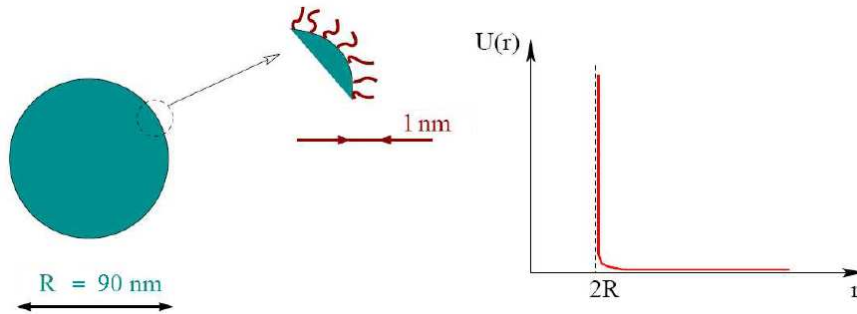
Figure 3.5: PMMA spheres coated with poly-12-hydroxystearic acid: entropic forces avoid aggregation.

was performed. Preparation of more concentrated sample was carried out by centrifugation and subsequent elimination of the resulting top layer of decalin.

Sample up to $\Phi \simeq 0.45$ were liquid or gel-like, therefore they can be flown through microfluidics devices. Higher concentration samples reached a solid vitrified phase, clearly unusable in our experiments. A phase diagram as a function of sample concentration is reported in figure 3.6, taken from [3].

As we can see, when concentration goes over a certain value an hard-spheres suspension becomes either gel or solid; therefore we can observe a disorder-order transition from random to crystalline phases, driven by entropy. Let's consider the concentration labelled with "RCP"; it indicates the most dense random arrangement of particles, namely the "Random Close Packing", which occurs at $\Phi \simeq 0.64$: in this situation particles are not free to move, the dynamic is completely arrested, therefore they have any free volume entropy left.

We expect the system to reach the state with the highest entropy, and this state can be the crystalline one, which indeed has lower configurational entropy, but higher free volume entropy: the total entropy of the crystalline phase can be higher then the one of glassy state (figure 3.7).

The viscosity of the sample was also measured, leading to a value of
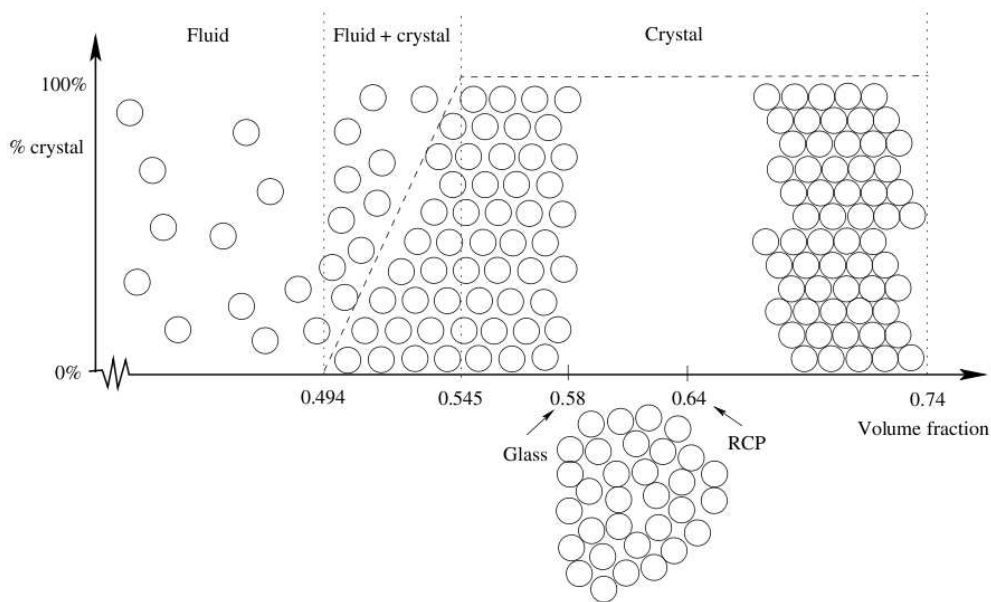
Figure 3.6: Phase diagram of PMMA sterically stabilized hard spheres, as a function of volume fraction [3]. The system can reach crystalline or glassy states.

$2.6cP$ at $298K$: water at the same temperature has a viscosity of $0.89cP$. This measurement was carried out using a U-tube viscometer, calibrated with water.

3.3.1   Brownian dynamics: measuring D_0 with DLS

In order to make a complete analysis of the dynamics of the sample through an XPCS experiment, the Einstein-Stokes diffusion coefficient D_0 is needed. To measure it, we could try to perform XPCS on a very diluted sample: the signal provided is, unfortunately, too low to measure correlation functions with a sufficiently high Signal-to-Noise ratio. On the other hand, recalling that in concentrated samples $D(Q)$ tends to D_0 as Q increases, we could try to measure it with XPCS at higher values for QR: this is not
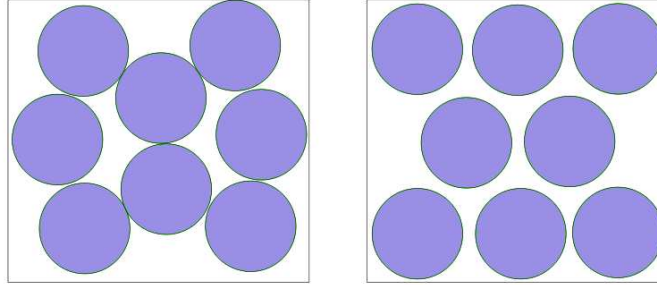
Figure 3.7: Entropy of hard spheres: the system on the right has higher total entropy, despite being more ordered, because it has higher free-volume entropy [3].

possible with the current experimental setup at ID10A. We must find another way: a standard technique as Dynamic Light Scattering, which is the same technique as XPCS but performed using visible light, provides enough photons to measure D_0 on a very diluted sample.
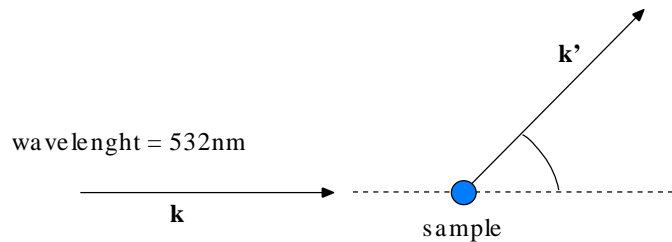

Figure 3.8: Dynamic Light Scattering: experimental geometry.

In a sample with concentration around 1%, colloidal particles move in a Brownian way: thus, correlation functions are given by equation (2.25). A simple exponential fitting leads to the desired measurement. The measure was repeated at different scattering angles, therefore D_0 was expressed as a function of the exchanged momentum Q, which is given by:

$$Q = \frac{4\pi n}{\lambda} \sin \frac{\theta}{2}$$

where $n = 1.48$ is an estimation of the reflectivity index of a mix of cis-trans decalin, and θ is the scattering angle.
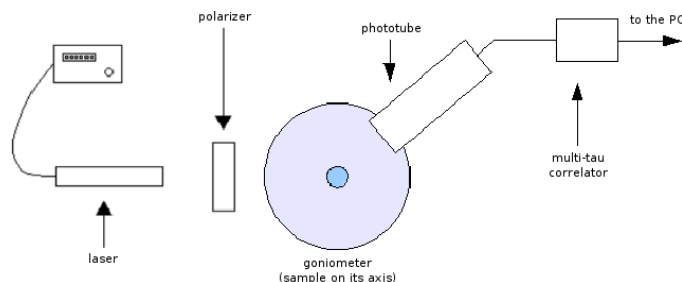
Figure 3.9: Dynamic Light Scattering: experimental setup.

As light sources we used two lasers, a red one and a green one, with wavelength respectively equals to $532nm$ and $633nm$. After hitting the sample, kept in a cuvette placed in the center of a goniometer, scattered light was detected by a phototube fixed to the goniometer itself, at around $30cm$ from the center. Then, the signal was sent to an hardware multi-tau correlator, and then to a PC (figure 3.9).

D_0 as a function of the exchanged momentum Q is reported in figure 3.10.

As a control test, we measured D_0 for a sample made of ASM361 hard spheres in cis-decalin: results are reported in figure 3.11.

	η	D_0
decalin	2.6cP	$0.899\mu m^2/s$
cis-decalin	3.2cP	$0.735\mu m^2/s$

The difference in viscosity between our mixed decalin and cis-decalin causes the difference in the measured diffusion coefficients reported in figures 3.10 and 3.11. Therefore, we have a crossed control over our viscosity measure. We can now cross-check viscosity and DLS measurements: from D_0 measurements, and given for cis-decalin a viscosity of $3.2cP$, we have an expected value for the viscosity of our mixed decalin of $2.6cP$, in perfect agreement with the value we measured using a viscometer. Measurements were performed at room temperature, 24^oC.
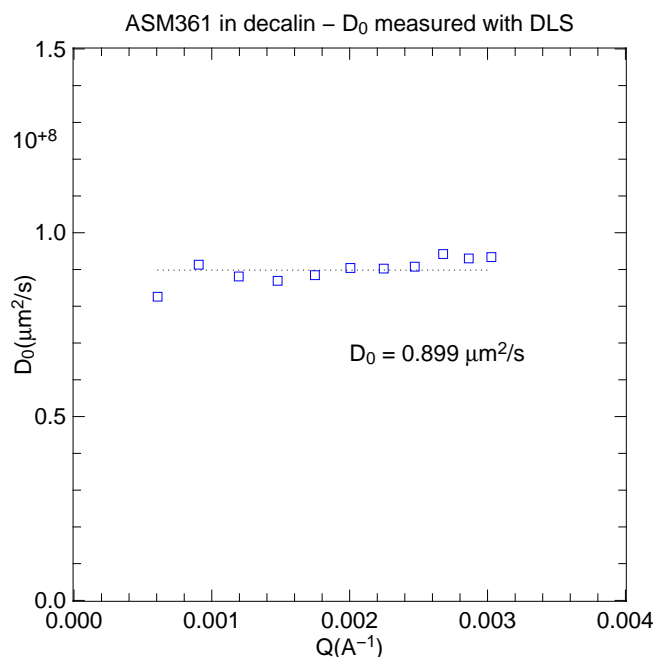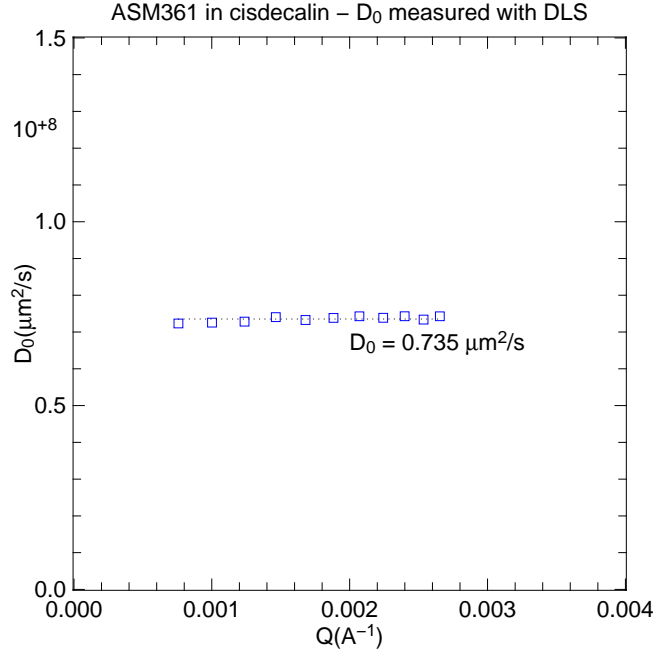
Figure 3.10: ASM361 hard spheres in decalin, very diluted sample: Einstein-Stokes coefficient measured with DLS

3.4 Flow devices for SAXS and XPCS

Flow devices characterized by a radius in the millimetre range can be easily build using cheap materials like kapton tubes, a very common material. Using T connections and tubes of different radius, it is possible to mix reactants directly in the flow device: the reaction begins in a precise position in the tube, mapping its time evolution in space and then opening up the way to time-resolved studies. One of the main advantages of millifluidics devices is that shear flow is automatically achieved because of the reduced diameter: no turbulence is present at reasonable flow rates.

While, as we will see, static properties of the suspension are not influenced by the presence of the flow because of the spherical symmetry of the particles, investigation of sample dynamics under flow requires some mathematical discussions; the contribute to the correlation functions given by the component of motion introduced by the experimental setup must be sepa-

Figure 3.11: ASM361 hard spheres in cis-decalin, very diluted sample: Einstein-Stokes coefficient measured with DLS

rated from the one which rises from particle intrinsic motion. This derivation is carried out in [24] under the hypothesis of uniform shear rate, in other words a parabolic profile of the velocities in the tube. The correlation function can be factorized into three different components, corresponding to different, statistically-independent physical origins: **thermal diffusion** of the colloids, **transit time** through the scattering volume, and **shear**;

$$|g_1\left(\vec{q},t\right)|^2 = |g_{1,D}\left(\vec{q},t\right)|^2 + |g_{1,T}\left(\vec{q},t\right)|^2 + |g_{1,S}\left(\vec{q},t\right)|^2. \qquad (3.10)$$

Considering that the experimental setup is characterized by a preferred direction, the one defined by the flow, it is useful to separate the exchanged momentum into two components, parallel and perpendicular to flow: $\vec{q}_{||}$ and $\vec{q}_\perp$.

When flow is not present, particle's thermal diffusion is Brownian, therefore the corresponding correlation function is a simple exponential:

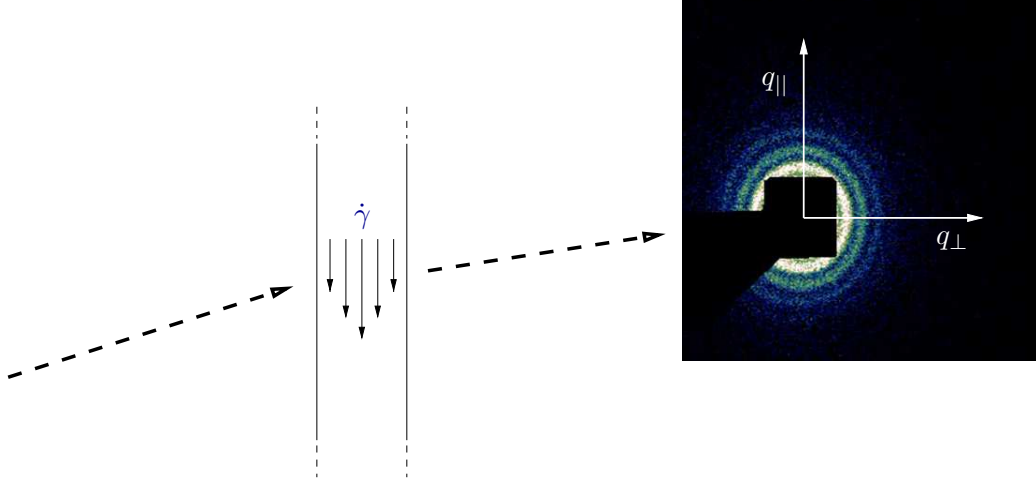$$|g_{1,D}\left(\vec{q},t\right)|^2 = \exp\left[-2Dq^2t\right]. \qquad (3.11)$$

Figure 3.12: Scattering geometry during a flow experiment: correlation functions change along difffernt directions as parallel or perpendicular to the flow.

The presence of shear flow erases the isotropy of this function, introducing a q-direction dependence:

$$|g_{1,D}\left(\vec{q},t\right)|^2 = \exp\left[-2Dq^2t\left(1 - \frac{q_{||}q_{\perp}}{q^2}\dot{\gamma} + \frac{q_{||}^2}{3q^2}(\dot{\gamma}t)^2\right)\right]. \qquad (3.12)$$

Transit time effect consists in a modification of the correlation due to the fact that, because of the flow, new particles enters the scattering volume while other particles are going out with a frequency $\nu_{tr} = v/h$, where v is the mean velocity of the sample in the tube and h is the perpendicular size of the scattering volume. The contribution of this effect is linked to the beam profile, scanned by the flowing particles; if this profile is approximated by a Gaussian curve, we obtain

$$|g_{1,T}\left(\vec{q},t\right)|^2 = \exp\left[-(\nu_{tr}t)^2\right]. \qquad (3.13)$$

The shear-rate effect, finally, is due to the fact that the particles do not have the same velocity when $\dot{\gamma}$ is not zero. Therefore Doppler-shifts are observed in the frequency of X-rays scattered from particles with different velocities. In order to obtain an analytical form for this contribution to the correlation

function, a double integral over the scattering volume on pairs of particles needs to be solved; the solution is:

$$|g_{1,S}(\vec{q}, t)|^2 = \frac{\sin q_{||} v_0 t}{q_{||} v_0 t} \qquad (3.14)$$

for uniform shear rate (Couette geometry), or

$$|g_{1,S}(\vec{q}, t)|^2 = \frac{\pi^2}{16 q_{||} v_0 t} \left| erf\sqrt{\frac{4i q_{||} v_0 t}{\pi}} \right|^2 \qquad (3.15)$$

for a parabolic velocity profile (Poiseuille flow).

It is important to note that the terms $q_{||} v_0$ is equal to the scalar product $\vec{q} \cdot \vec{v_0}$. When the exchanged momentum $\vec{q}$ is perpendicular to flow, the second and third terms in the exponent of equation (3.12) vanish, therefore (3.12) becomes equal to (3.11). In the same approximation, $|g_{1,S}(\vec{q}, t)|^2$ and $|g_{1,S}(\vec{q}, t)|^2$ are zero, while the term $|g_{1,T}(\vec{q}, t)|^2$ is usually negligible. Therefore, using an experimental geometry where the scattering vector is perpendicular to the flow is perfect in order to measure directly the dynamics of the sample, since the introduction of flow-induced effects is avoided.

In figure 3.13, reported in [24], the effects of flow over the correlation time τ are shown; τ was detected using a geometry where $\vec{q}$ was perpendicular to the direction of the flow itself. At low flow rates the q^2 dependence expected for Brownian dynamic is observed, while at higher flow the influence of both transit time and shear effects is detected.

During our experiment, a geometry with $q_{||} = 0$ was used: a perfect alignment is generally not achievable, thus shear induced effects were seen working at higher flow rates even in this configuration. Anyway, operating at low flow rates, the diffusive dynamics of the particles can be measured as in a normal experiment.
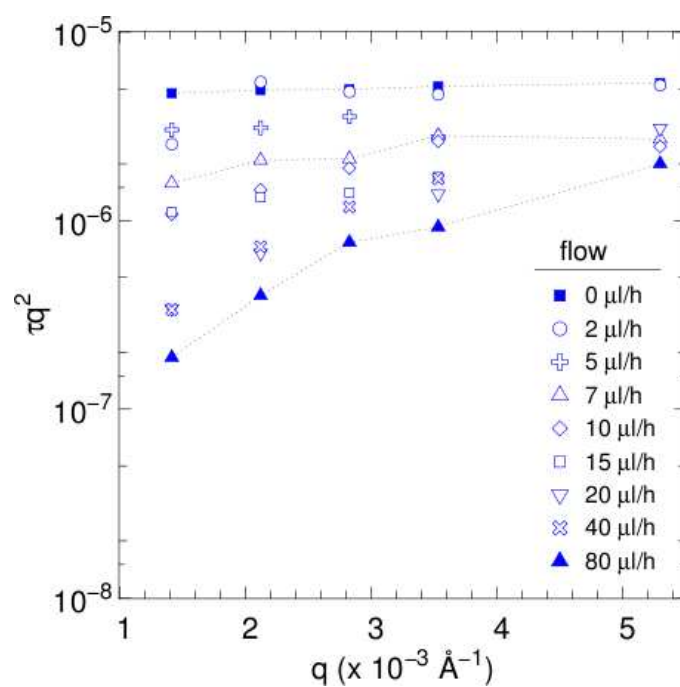
Figure 3.13: Correlation time τ multiplied by q^2, as a function of q, in a $q_{||} = 0$ geometry. At low flow rates, no influence is detected: therefore we are measuring the diffusive dynamics of the particles. From [24].

Chapter 4

Experimental Results

4.1 Structure of hard-sphere suspensions

After a first characterization of our colloidal suspension, having measured its viscosity and the Einstein-Stokes diffusion coefficient D_0, we started the analysis of its static and dynamical properties as a function of the concentration of particles, represented by the volume fraction Φ. The static characterization of our sample was performed by means of SAXS at the beamlines ID10A and ID02 of ESRF: in other words, our first aim consists of exactly knowing what kind of suspension we are looking at. As previously explained, the size distribution of particles and the volume fraction of the suspension are assessable through this technique.

During sample preparation, particular care was paid to avoid any alteration of the mean radius and polydispersity. Since preparing concentrated samples by centrifugation may lead to a gradient of sizes, and during the subsequent elimination of the upper layer of solvent, smaller particles can be eliminated as well, centrifugation was not applied.

As a detector we used the CCD, because of the large exchanged momentum range achievable in a single shot and of its high resolution: with a judicious choice of sample-to-detector distance ($d = 2.19m$) we could measure in the Q range from $Q \simeq 0.001\mathring{A}^{-1}$ up to $Q \simeq 0.03\mathring{A}^{-1}$.
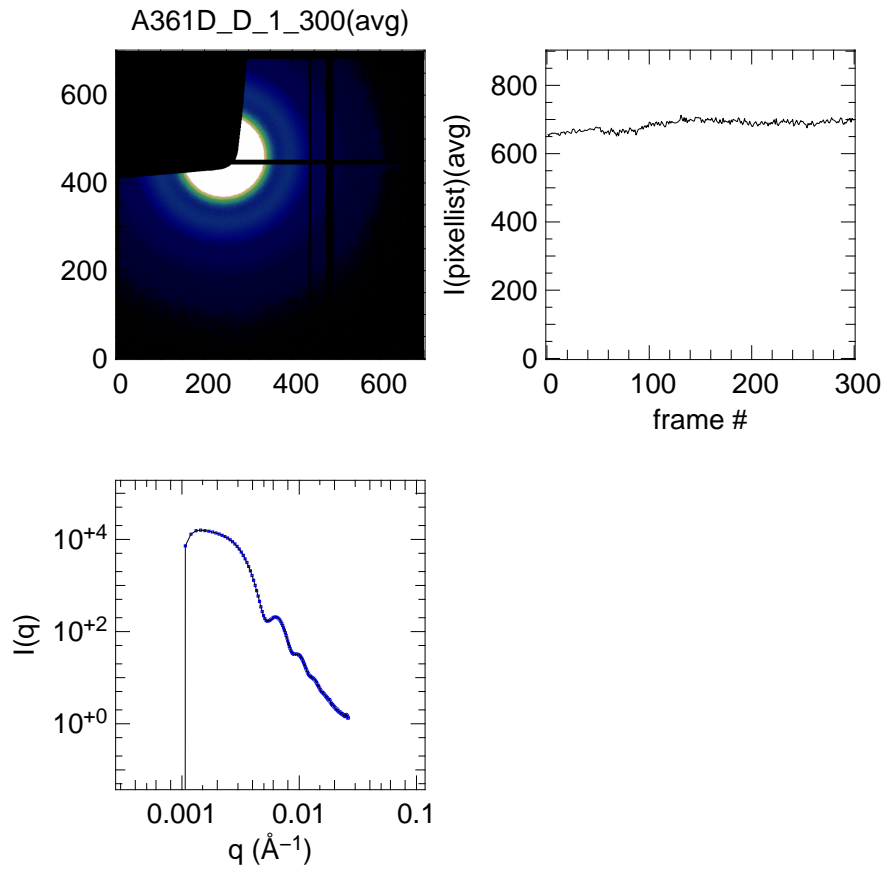
Figure 4.1: SAXS measurement. Top-left: 300 images were taken, then averaged. Top-right: the average intensity constancy is checked. Bottom: Saxs measurement; the image radial average as a function of Q.

A beamstop is interposed between the detector and the direct beam to avoid damage. Since the low-Q limit is determined by the beamstop position relative to the direct beam, sometimes the measurement starts from a too high value of Q, losing fundamental informations on the structure of the sample. In these cases, we integrated the SAXS patterns with those measured by the point detector, although its resolution is lower. Using CCD (figure 4.1), normally 300 frames were collected to compensate its limited dynamical range. Frames were then summed together pixel by pixel, obtaining a single pattern. A radial average is performed around the centre of the beam, which is obtained taking an image without the beamstop and with attenuators into

the beam path. Bad pixels were masked, and a measurement without light is subtracted in order to eliminate spurious effects. Intensity as a function of Q can be fitted with the models described in chapter 2.1, giving access to all these parameters that describe the sample from a static point of view, thus obtaining the structure factor S(Q), which will be useful in the successive analysis. The importance of this factor, containing information on interparticle interactions, increases as the volume fraction Φ grows, while it is nearly equal to one at low concentrations.

It is not yet possible to directly compare the results of our SAXS experiment with the model for the scattered intensity, since we need to subtract the scattering contribution due to both the solvent and the kapton tubes. Then, we must add to the model the influence of instrumental resolution over the detected intensity. This is usually done in literature by performing a convolution of the hard-sphere form factor with a Gaussian profile, whose width is linked with the uncertainty over the exchanged momentum.

Data are fitted with the expression, reported in chapter 2.1,

$$I(Q) = K \, S(Q) \, P(Q) \tag{4.1}$$

where K is a scale factor, $P(Q)$ is the form factor of a sphere and $S(Q)$ is the structure factor. The mean value $\overline{R}$ and the standard deviation $\sigma = \overline{R}/\sqrt{Z+1}$ of the particle's radius R are parameters of the fits, while sample volume fraction Φ is a manually varied parameter. Structure factor determination is the main goal of this measurement: it can be obtained computing the ratio between $I(Q)$ and the scaled form factor $K\,P(Q)$, convoluted with a Gaussian profile; we can call it "measured structure factor". This curve can be compared with the $S(Q)$ expected, in the Percus-Yevich approximation, for spherical particles interacting as hard-spheres.

Another model we could have used was the analytical expression for $I(Q)$, reported in [4], where the factorization between $S(Q)$ and $P(Q)$ is not made: a fit performed using said model does not provide a determination of the structure factor, although R and Φ can be determined with higher precision. Since the core-shell particles model does not lead to significant improvements

despite the higher number of parameters, as previously mentioned in chapter (2.1.2), it is not used in this analysis and the Percus-Yevich hard-sphere model is the only one considered.

In figures 4.2a, 4.3a, 4.4a, 4.5a, 4.6a, 4.7a and 4.7a SAXS patterns and fits are reported for samples characterized by a volume fraction up to around 50%. Figures 4.2b, 4.3b, 4.4b, 4.5b, 4.6b, 4.7b and 4.8b contain both the "measured" and the expected structure factor.
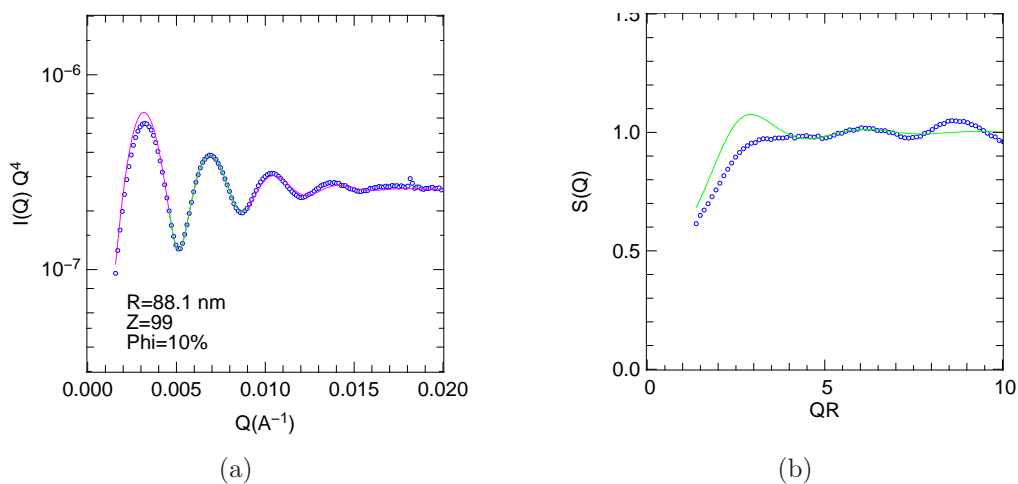

(a)   (b)

Figure 4.2: A631D_D sample. a) Best fit over the green region of the curve, with $R = (881\pm3)\mathring{A}$; $Z = 99\pm6$; $\Phi = 9.5\%$; b) Structure factor; the continue curve is the expected S(Q), the dotted one is the "measured structure factor".

As we can see, the pattern is better fitted in the high Q region, while there are some problems in the low Q region, the problem being that either the low Q region or the high Q can be fitted well. Our attempt to overcome this problem by doing a convolution of the model with a Gaussian profile is not sufficient. Trying to fit the curve profile for $Q > 0.005\mathring{A}^{-1}$ in a better way, gives a wrong height of the structure peak. On the other hand, trying to get a better fit in the low-Q region leads to bad results in the remaining part of the curve; a balanced approach is therefore needed. We decided to fit only over the first two maxima after the structure peak. Since in the following analysis the main information we will need is the peak's position
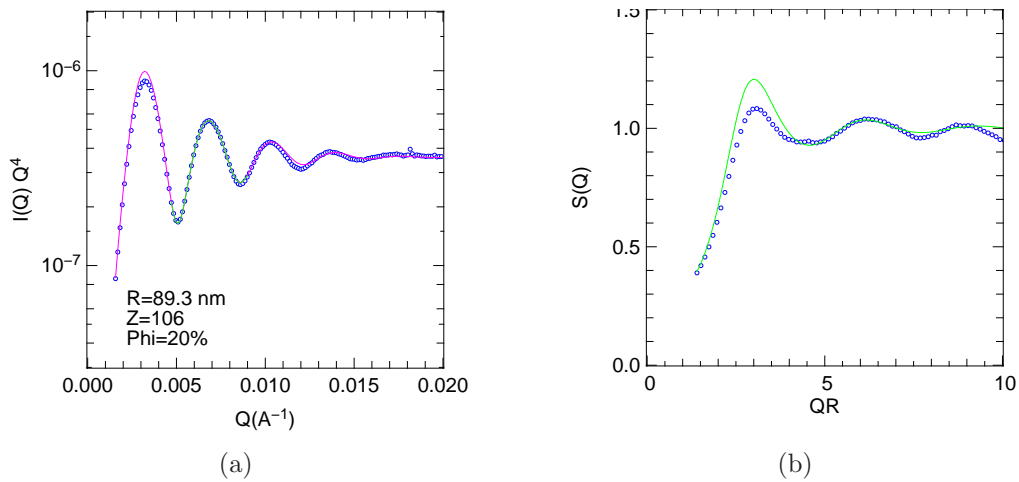
Figure 4.3: A631D_C sample. a) Best fit over the green region of the curve, with $R = (893 \pm 3)\mathring{A}$; $Z = 105 \pm 6$; $\Phi = 19.5\%$; b) Structure factor; the continue curve is the expected S(Q), the dotted one is the "measured structure factor".
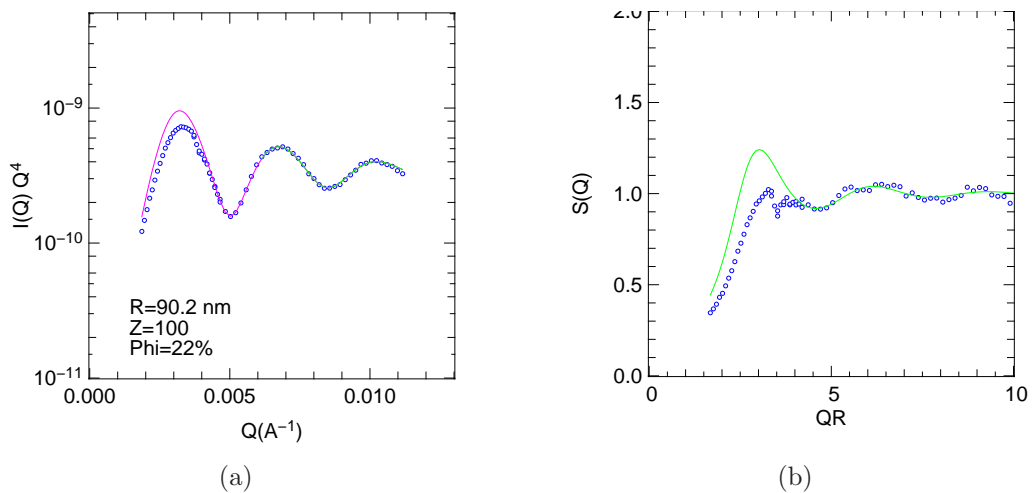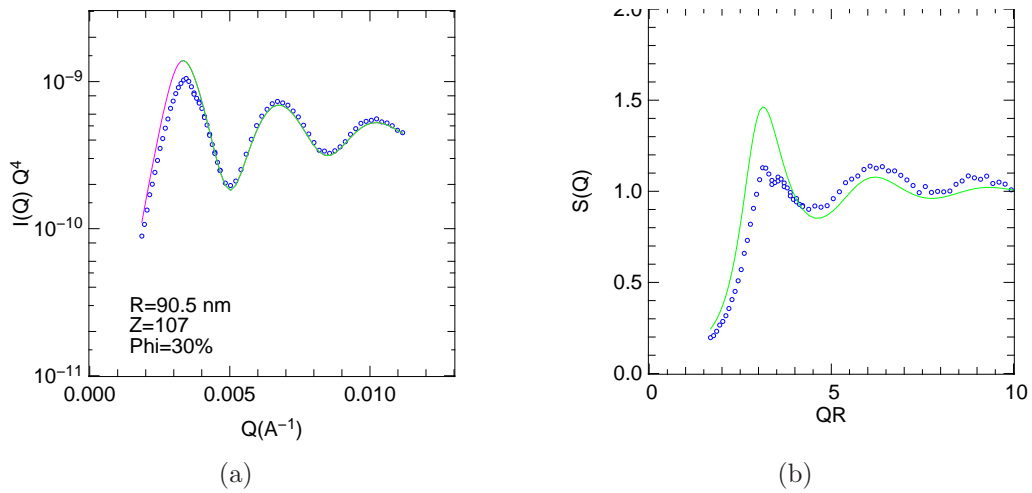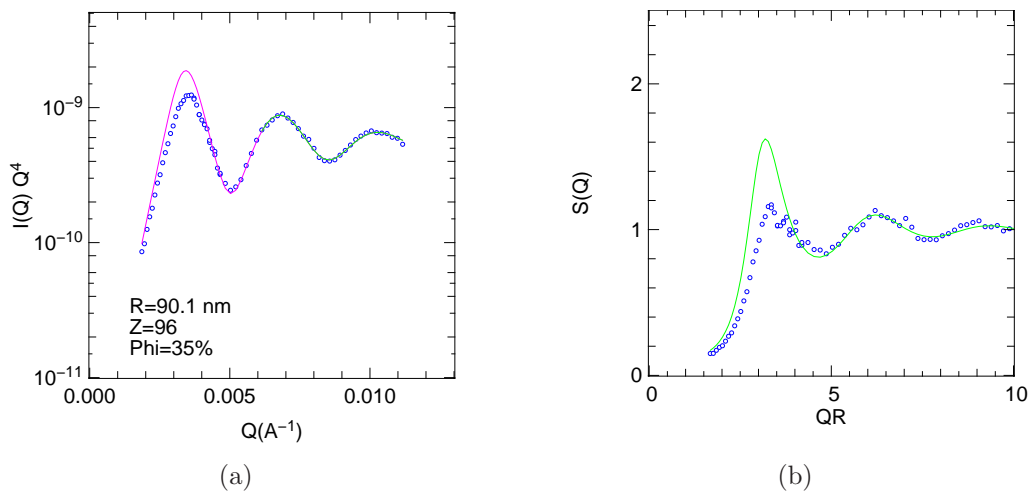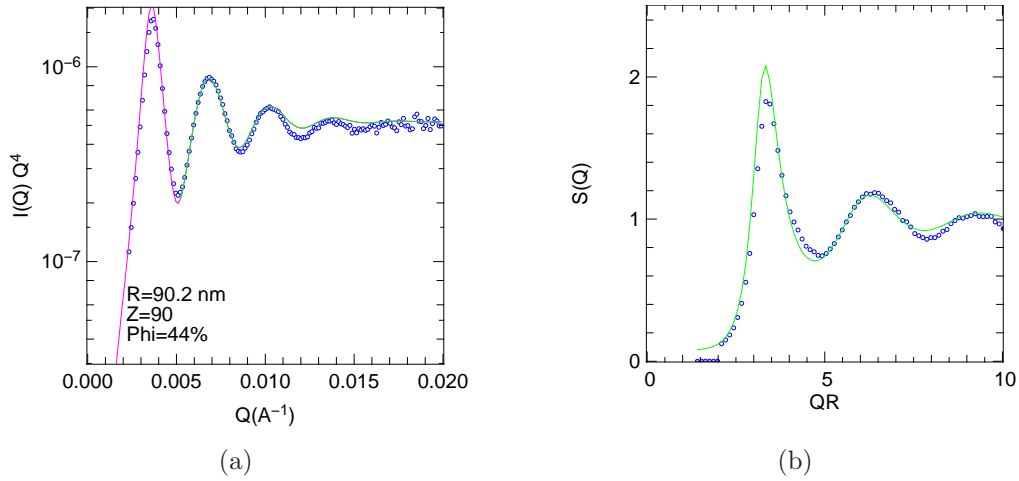

Figure 4.4: A631D_E sample. a) Best fit over the green region of the curve, with $R = (908 \pm 3)\mathring{A}$; $Z = 99 \pm 4$; $\Phi = 21.5\%$; b) Structure factor; the continue curve is the expected S(Q), the dotted one is the "measured structure factor".

Figure 4.5: A631D_P sample. a) Best fit over the green region of the curve, with $R = (905 \pm 3)\mathring{A}$; $Z = 107 \pm 4$; $\Phi = 30.5\%$; b) Structure factor; the continue curve is the expected S(Q), the dotted one is the "measured structure factor".

Figure 4.6: A631D_F sample. a) Best fit over the green region of the curve, with $R = (901 \pm 3)\mathring{A}$; $Z = 96 \pm 2$; $\Phi = 35.2\%$; b) Structure factor; the continue curve is the expected S(Q), the dotted one is the "measured structure factor".

(a)

(b)

Figure 4.7: A631D_A sample. a) Best fit over the green region of the curve, with $R = (901 \pm 3) \mathring{A}$; $Z = 90 \pm 5$; $\Phi = 44\%$; b) Structure factor; the continue curve is the expected S(Q), the dotted one is the "measured structure factor".
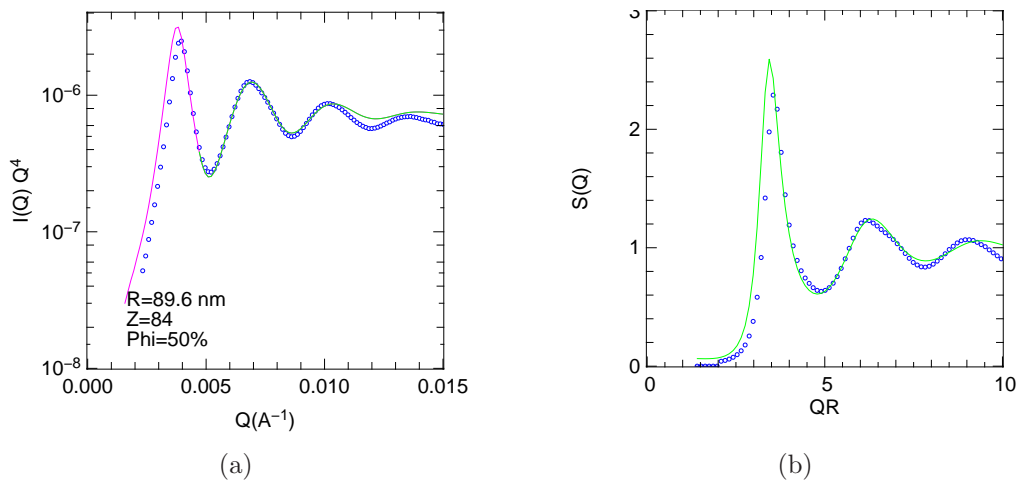

(a)

(b)

Figure 4.8: A631D_G sample. a) Best fit over the green region of the curve, with $R = (896 \pm 5) \mathring{A}$; $Z = 84 \pm 8$; $\Phi = 50.5\%$; b) Structure factor; the continue curve is the expected S(Q), the dotted one is the "measured structure factor".

only, and we can therefore accept some discrepancy in the determination of the intensity, we tried to obtain compatible values of R and Z for every sample. Concentration estimations comply with the expected values.

sample	nominal Φ	Φ	R (Å)	Z	σ (Å)
A361D_D	10%	9.5%	881 ± 3	99 ± 6	88 ± 3
A361D_C	19%	19.5%	893 ± 3	105 ± 6	86 ± 3
A361D_E	22%	21.5%	908 ± 3	99 ± 4	90 ± 2
A361D_F	30%	30.5%	905 ± 3	107 ± 4	87 ± 2
A361D_P	35%	35.2%	901 ± 3	96 ± 2	91 ± 2
A361D_A	45%	44%	901 ± 3	90 ± 5	94 ± 3
A361D_G	50%	50.5%	896 ± 5	84 ± 8	97 ± 5

We obtained a "measured" $S(Q)$ different from the Percus-Yevich theoretical prediction for hard spheres. This is probably an indication that hard spheres approximation fails for our system, although an alternative explanation could be related to experimental problems at low Q. Anyway, an indication that our sample is effectively made of spheres comes from the comparison of the so-called hydrodynamical radius $R_h = \frac{k_B T}{6 \pi \eta D_0}$ with the radius obtained from SAXS. For our sample, $R_h \simeq 930$ Å: since it is slightly greater than the R measured by fitting data with the hard sphere model, our sample likely does not contains broken spheres of other non-spherical particles.

4.2 Dynamics of hard-sphere suspensions

The second part of this work is focused on particle motion and interactions. Since we are performing measurements in a region of the reciprocal space where $QR < 10$, we are mainly considering interactions between particles separated by a distance $d > \frac{2\pi R}{10} = 0.6R \simeq 60nm$. The dynamics of nanoparticles in a solvent displays three different regimes:

- the ballistic regime, when we consider a time short enough over which the colloidal particle behaves, after a collision, as a free particle;

- the Brownian "short time" regime, when the particle moves around its equilibrium position: in this case the motion is diffusive and has not been slowed down by interparticle interactions;

- a long-time regime with diffusive motion, when the particle moves on even greater distances and its motion is affected by the so-called "cage" effect due to the presence of surrounding particles.

This work is focused only on the "short-time" regime. The separation is given by the time-scale characterizing the diffusion, and by its confrontation with relevant time-constants defined by some static parameters like radius (R), mass of the particle (m), temperature (T) and viscosity (η). We can define two relevant time-constants:

- the first is the so-called Brownian relaxation time, $\tau_B = mD_0/k_BT \simeq 1ns$: this is the time a particle takes, after a collision, to lose an energy comparable with the thermal excitation energy k_BT while interacting with the solvent. Therefore, it is the time after which the definition of the diffusion coefficient is meaningful;

- the second one is the time a particle needs to diffuse freely over a distance equal to its radius, and can therefore be defined as $\tau_R = R^2/D_0 \simeq 9ms$.

When $\tau_B < \tau < \tau_R$, we have the "short time" regime; the "long time" one occurs when $\tau > \tau_R$. The investigation of the "ballistic" regime is not possible by XPCS, since detector that can reach detection times shorter than τ_B are not available. In brief, we are looking, during a time shorter than the time needed to diffuse over a distance comparable with the radius, at the dynamics and interactions among particles separated by distances much greater than their radius.

XPCS measurements of the correlation functions were performed at various values of Q, corresponding to a region up to the second relative maximum

in the intensity profile, where $QR < 6$. On the one hand, in very low concentration samples the correlation function decay is an exponential:

$$g^{(2)}(\tau) = 1 + \left| \frac{F(\vec{Q}, t)}{F(\vec{Q}, 0)} \right|^2 = 1 + e^{-2D_0 Q^2 t}.$$

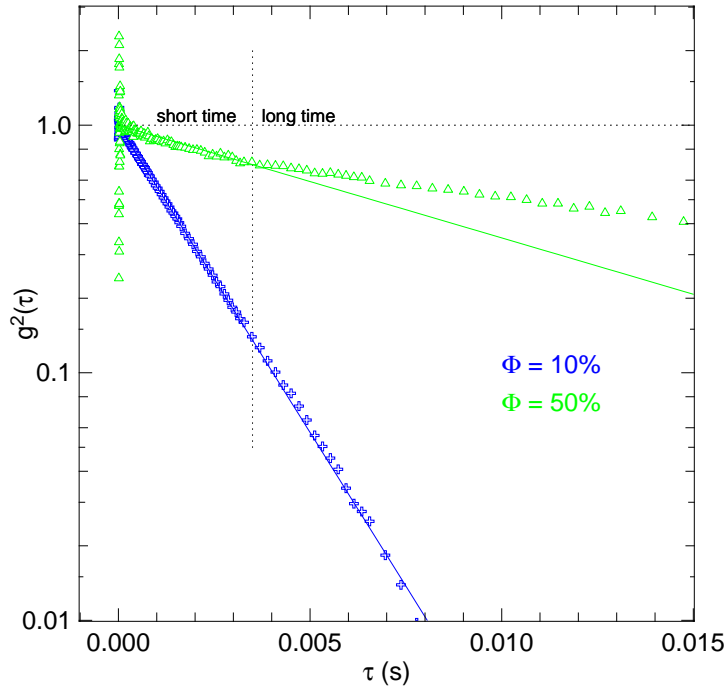where D_0 is the usual Einstein-Stokes coefficient.

Figure 4.9: Correlation functions at $\Phi = 10\%$ and $\Phi = 50\%$. In the high-Φ curve, two different time-scales are visible: the fit is performed only at short times, in the first region.

On the other hand, at higher concentrations, this no longer applies: a Q-dependence has to be introduced for the diffusion coefficient $D_S(Q)$. If we plot, like in figure 4.9, a correlation function measured at a high concentration in a semi-logarithmic scale, we can see that it presents the two different time scales. This recalls the presence of the two different diffusion regimes, previously referred to as "short time" and "long time" regimes, discriminated by the characteristic time τ_R. Therefore, through exponential fitting over

the $\tau < \tau_R$ region we obtain a measure of $D_S(Q)$. This measurement was performed at different flow-rates, ranging from zero up to $800 \mu L/h$ and even $1600 \mu L/h$. If results obtained with small flow-rates are compatible with those observed without flow, then neither cavitation nor ageing effects are present. Moreover, if low-flow-rate data are consistent with one another while the flow-zero curve shows a different behaviour, this means that the latter is not completely trustworthy. High-flow-rate data usually present flow-induced effects, and are therefore not suitable for the subsequent analysis.

While analysing $D_S(Q)$, it is useful to set aside the contribution of direct interactions, represented by the structure factor $S(Q)$ we obtained through SAXS analysis. Since we are looking at times shorter than the time τ_R necessary to diffuse over a distance of a particle radius, we can consider nanoparticles in motion just around their equilibrium position during the measurements. In this situation, structural and hydrodynamical effects can be separated by a factorization of $D_S(Q)/D_0$, as reported in [5]:

$$\frac{D_S(Q)}{D_0} = \frac{H(Q)}{S(Q)} \qquad (4.2)$$

D_0 was measured by DLS, $S(Q)$ by SAXS and $D_S(Q)$ by XPCS, we have a measurement of the so-called hydrodynamic function $H(Q)$, which represents the interparticle interaction due to solvent motions as effect of the movement of the other particles and of the particle itself. A model for $H(Q)$ as a function of suspension volume fraction has been developed by Beenakker and Mazur: in reference [6] they studied the self-diffusion contribution giving rise to a Q independent term, while in [7] many-body hydrodynamics interactions are taken into consideration leading to the Q-dependent contribution. The calculation is lengthy and fairly complicated, and it is not reported here: anyway, the final expression requires numerical integration which was performed as part of the tasks of the present thesis work. The results are reported in figure 4.10, similar to figure 2 in [7].
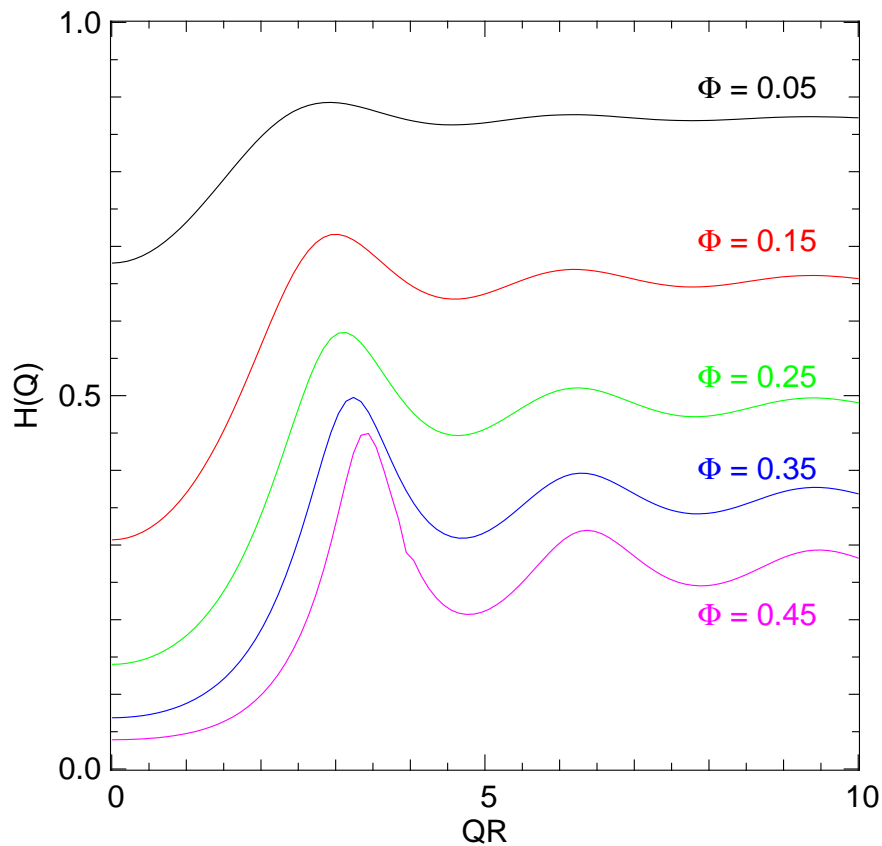
Figure 4.10: Model for the hydrodynamic function at different concentrations.

4.2.1 Results

In figures from 4.11 to 4.17, each one referring to one sample, $D_S(Q)$ normalized to the Einstein-Stokes constant is reported, and the corresponding structure factor is displayed as well. Data taken with sample flowing at $100 \mu L/h$ are highlighted since this flow-rate fulfils the requirements stated above: cavitation and ageing effects are avoided.

Note that in each figure the first relative minimum corresponds to the position of the maximum in S(Q), Q_{max}: this means a slowing down of the dynamics in correspondence of the structure's peak. The suspension's density fluctuations with wavelength $\frac{2\pi}{Q}$ decay in an exponential way, except for those
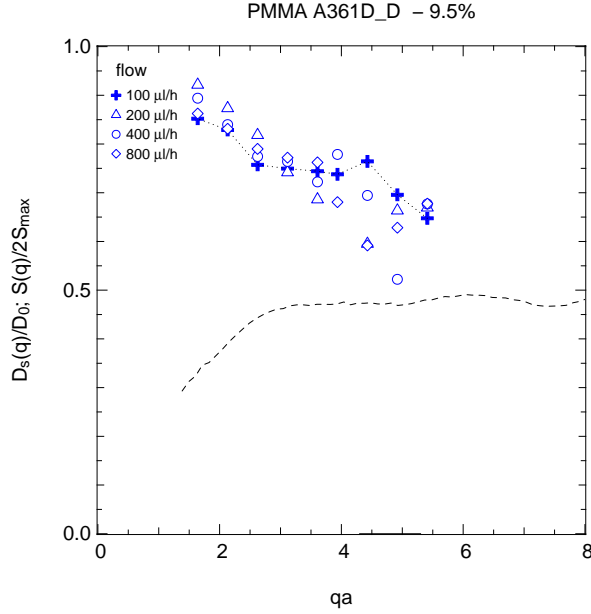
Figure 4.11: A361D_D sample, $\Phi = 9.5\%$. Q dependence of $D_S(Q)$ normalized to D_0. The measured structure factor $S(Q)$ is reported for comparison.

with a wavelength similar to $\frac{2\pi}{Q_{max}}$ that are more likely to persist: their decay takes place with a slower characteristic time. This effect is closely resemblant the so called "de Gennes narrowing", well known in the literature [8]. It consists in an energy narrowing of the quasielastic neutron scattering as a function of the exchanged momentum Q in correspondence of the maximum in the structure function S(Q). Its physical origin relies on the fact that the dynamic of the system tends to be slower in correspondence of its structural periodicities, in other words, the system tends to preserve its coherence at that particular Q value by reducing the corresponding dynamics.

As we can see in figures 4.11 and 4.12, the low concentration samples "A361D_D" and "A361D_C" show problems of data dispersion among curves relative to different flow-rates. In particular, an oscillation pattern common to every flow-rate is not present, while higher concentration samples do not present this problem and the oscillation patterns of $S(Q)$ and $D_S(Q)$ are in clear agreement. The "A361D_C" sample was not considered in further analysis of the hydrodynamic function $H(Q)$, since its concentration $\Phi \simeq$
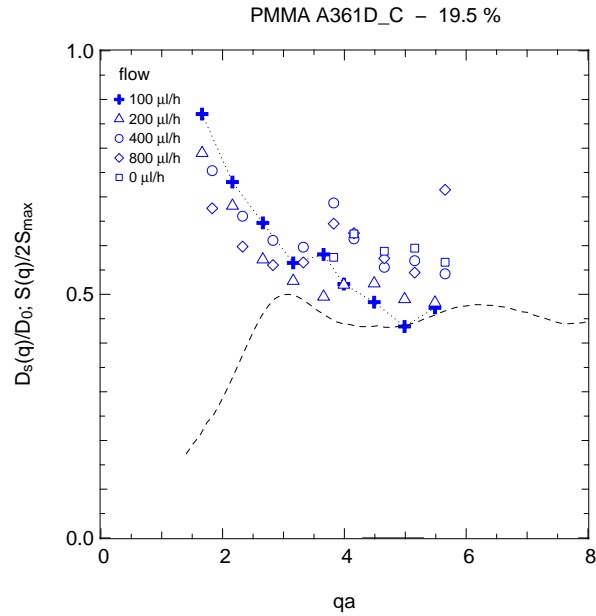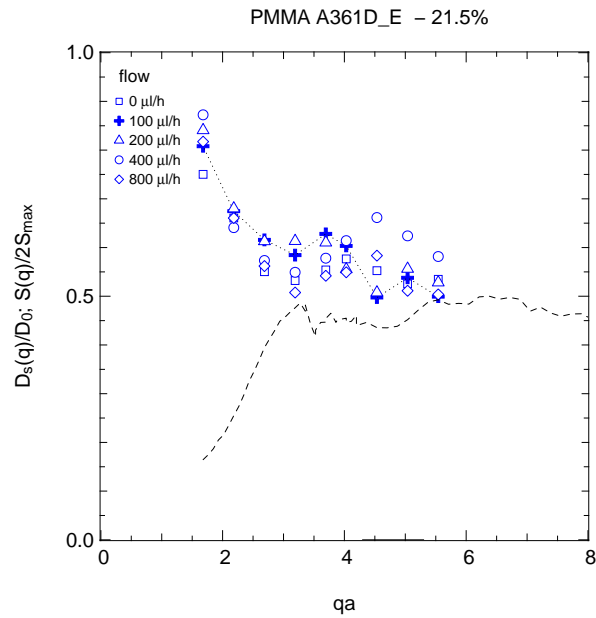
Figure 4.12: A361D_C sample, $\Phi = 19.5\%$. Q dependence of $D_S(Q)$ normalized to D_0. The measured structure factor $S(Q)$ is reported for comparison.

Figure 4.13: A361D_E sample, $\Phi = 21.5\%$. Q dependence of $D_S(Q)$ normalized to D_0. The measured structure factor $S(Q)$ is reported for comparison.
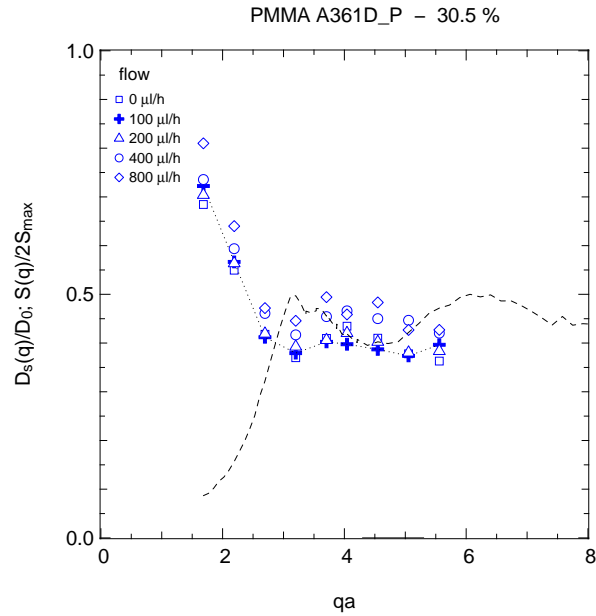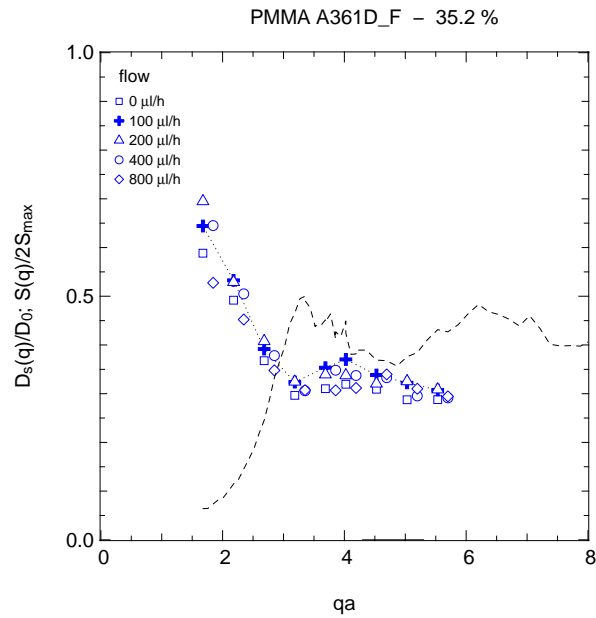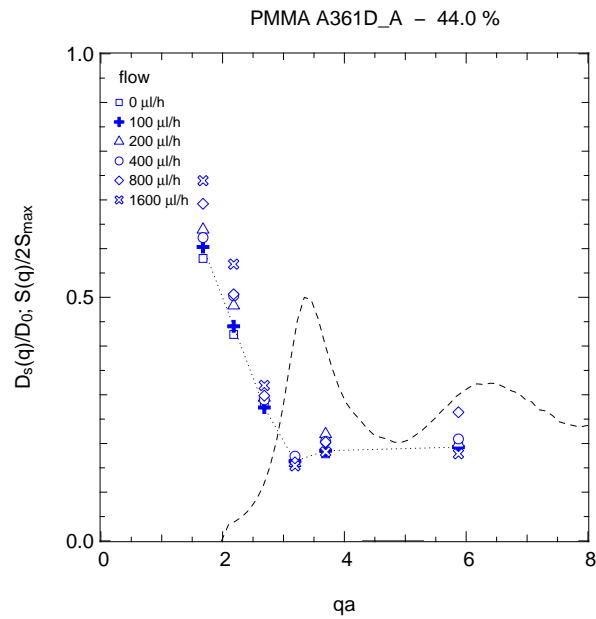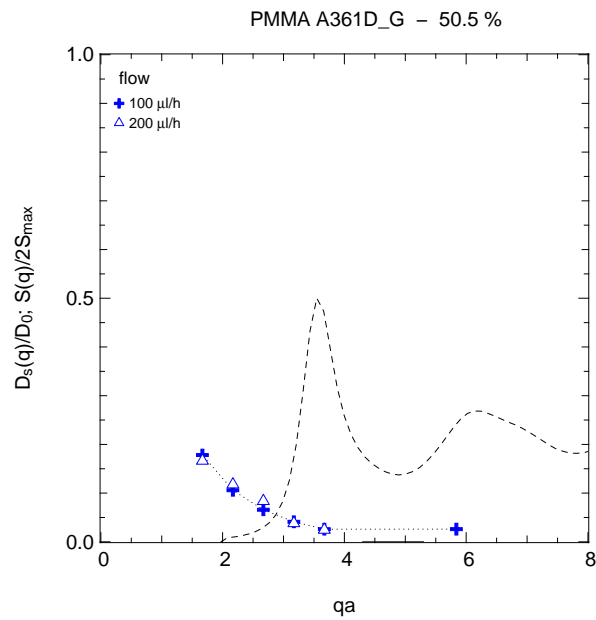
Figure 4.14: A361D_P sample, $\Phi = 30.5\%$. Q dependence of $D_S(Q)$ normalized to D_0. The measured structure factor $S(Q)$ is reported for comparison.

Figure 4.15: A361D_F sample, $\Phi = 35.2\%$. Q dependence of $D_S(Q)$ normalized to D_0. The measured structure factor $S(Q)$ is reported for comparison.

Figure 4.16: A361D_A sample, $\Phi = 44.0\%$. Q dependence of $D_S(Q)$ normalized to D_0. The measured structure factor $S(Q)$ is reported for comparison.

Figure 4.17: A361D_G sample, $\Phi = 50.5\%$. Q dependence of $D_S(Q)$ normalized to D_0. The measured structure factor $S(Q)$ is reported for comparison.

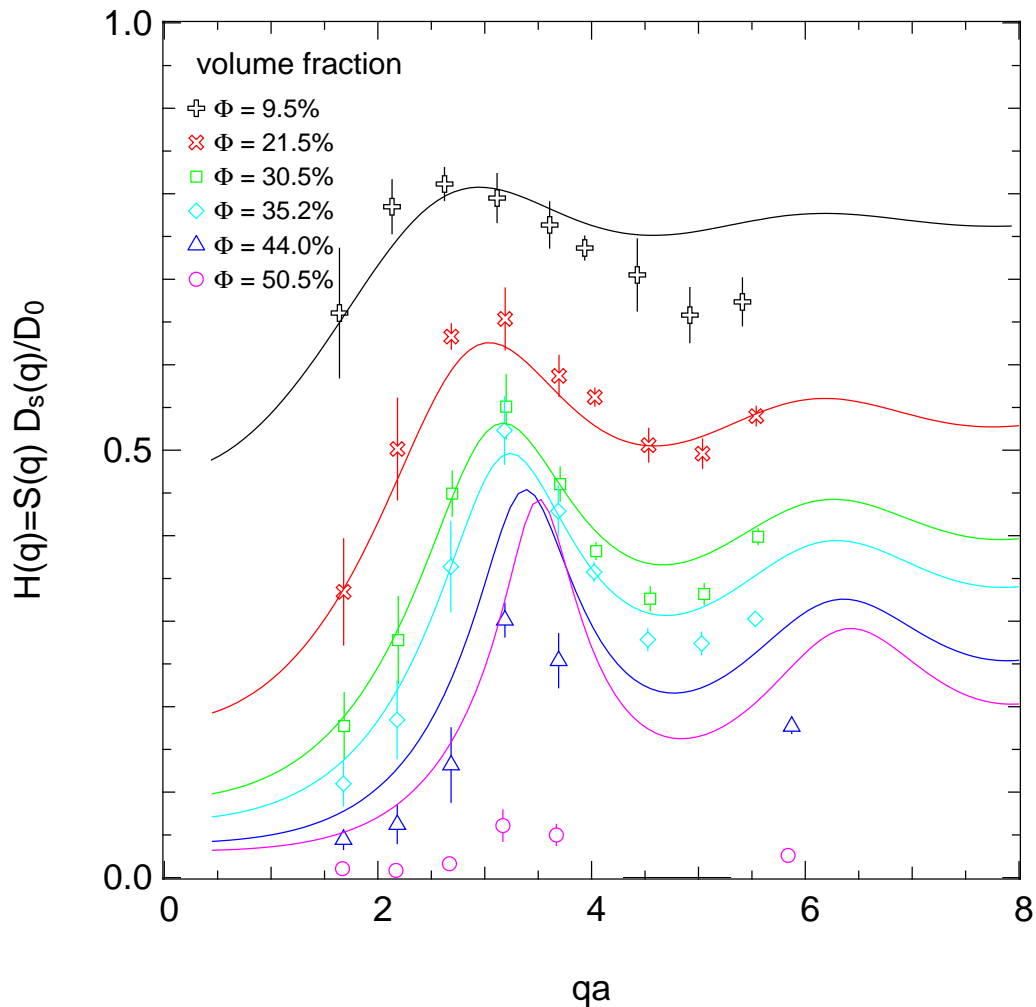19% was very similar to the one of the "A361D_E" sample, $\Phi \simeq 21\%$.

Figure 4.18: $H(Q)$ at different concentrations. The continuous lines represent Beenakker and Mazur's predictions. Error bars came from statistical analysis of correlation functions (chapter 3.2) and of $S(Q)$.

We can now calculate the hydrodynamic function $H(Q)$ introduced in equation (4.2) to represent every other contribution to the diffusion, in particular interactions through the liquid medium, called "hydrodynamical" in-

teractions. In figure 4.18 data measured at various concentrations relative to the $100\mu L/h$ flow-rate are reported. The sole exception is given by sample A361D_E since, although it is a low-concentration sample, in principle not affected by cavitation problems, it displays a Q dependence not compatible with the no-flow curve. For the A361D_E sample the no-flow points were used. These values of $H(Q)$ are compared to the theoretical curves calculated for the respective values of R, Z and Φ, following [6] and [7].

It is clear how at low concentration the predicted hydrodynamical function is fairly unstructured, while at high volume fractions the theoretical $H(Q)$ shows a first maximum at $QR \simeq 3$ and a subsequent minimum at $QR \simeq 4.5$; this behaviour is reasonably well reproduced by our experimental data. At $\Phi = 44\%$, the sample's dynamics begins to arrest, therefore we can see a clear deviation of data from the expected behaviour. At $\Phi = 50\%$ the sample is no longer fluid but it appears more like a gel, and obviously applying a theory developed for particles suspended in a liquid leads to completely wrong theoretical conclusions.

4.3 Future work on hard spheres dynamics

The results reported in this work are but a first step in the investigation of the dynamical properties of hard spheres. A further step forward could be represented by the analysis of the "long time" regime, defined in chapter 4.1. This task involves looking at the correlation functions in the region $\tau > \tau_R$, with particles travelling on longer distances and therefore being affected by the so-called "cage" effect. Moreover, the theoretical model which provides an expression for the hydrodynamic function $H(Q)$ is developed only for the "short time" regime, while a computational approach is not viable, because of the huge number of particles involved in this regime.

Chapter 5

Time-resolved studies in flow devices

In this section we report some applications of microfluidic techniques to time-resolved measurements or studies in a confined volume which I contributed to test and develop during my stay at ESRF under the supervision of Andrei Fluerasu from ESRF, working with Jean-Baptiste Salmon and Fanny Destremaut from Bordeaux CNRS, and with ID10A staff. Although not directly related to hard spheres dynamics, the following examples can show how microfluidics is powerful, an provide new ideas for further improvements.

5.1 Emulsion droplets: SAXS

Silica hard spheres are often used for calibration during XPCS experiments, because of their well-known Brownian behaviour in diluted solutions. In this section, a simple application of microfluidic devices is shown: a SAXS measurement of the static properties of a suspension of charge stabilized silica particles in water, by forming a droplet which is flowing in an oil stream (figure 5.1). We want to prove that performing this kind of measurements on a confined system is possible with a very simple experimental setup, and that the presence of the flow does not influence the results. The following

87

is also a good example of what kind of information can be obtained from a SAXS measurement even if information is missing, especially at very low exchange momentum.
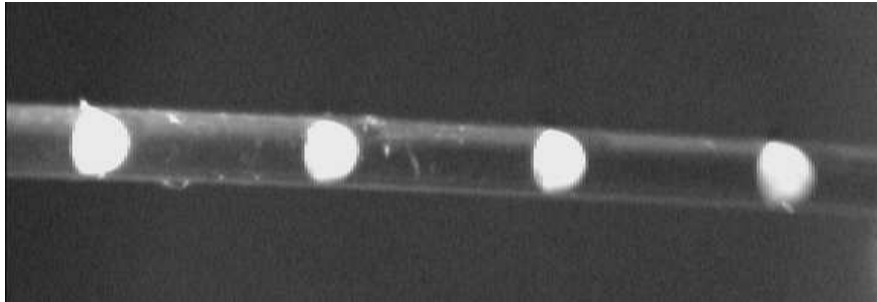

Figure 5.1: Droplets of sample flowing in oil, into a $1mm$ tube. Photo taken at ID10A.

We used silica particles (diameter $\simeq 0.5\mu m$) purchased from Duke Scientific Corporation, California, suspended in water. With three syringes, and a tube-in-tube-in-tube setup, the desired sample was formed directly into the flowing device, completely avoiding unwanted ageing effects and automatically defining the instant at which the components start to mix as $t_0 = 0$ (figure 5.2).

Sample droplets were formed with a frequency $f = 0.4Hz$; the sample was injected at various flow-rates using a first syringe, while water was added to the sample using a second one, reaching a total flow rate of $1ml/hour$. The volume of one droplet was obtained multiplying frequency and sample's flow rate.

Because of beamstop position, we have limited our analysis to $QR > 7$, hence S(Q) is constant. The diffracted intensity was fitted using only the form factor model for polydisperse particles from chapter (2.1.2).

In figure 5.3, the scattered intensities at various silica's flow rates are reported, along with relative fits. Increasing the flow rate of water, we could change he concentration of suspended silica particles. Then, the volume fraction was calculated using equation (2.8): the linear relation between the
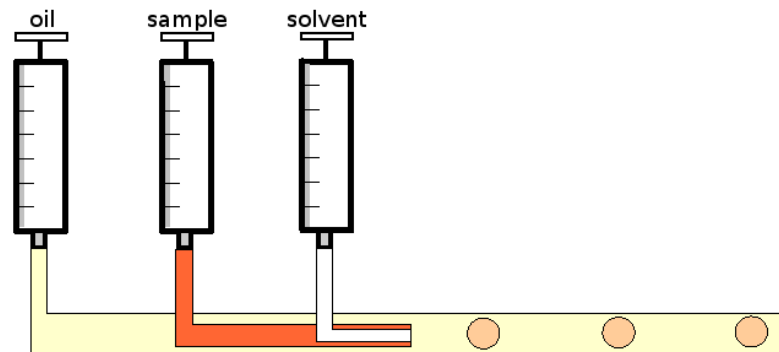
Figure 5.2: Triple syringe configuration was used in order to create flowing droplets of sample with concentration given by the ratio between the flow rates of stock sample and water.

concentration and the flow rate is clear.

This particular example demonstrates that performing SAXS on a droplet of sample flowing in a tube is possible, obtaining the same information we get during a usual experiment. Further developments of this technique include the study of a self-assembly process as it occurs: the process begin only when reactants are mixed directly in the tube by the three-syringe device, forming a bubble that starts to flow. Doing SAXS at different beam positions along the tube, we can obtain information about shape and dimensions of newly forming aggregates.

5.2 Gel formation

The aim of this second example of microfluidic experiment was to study the gel formation process. We used two syringes and a tube-in-tube configuration similar to the one in figure 5.2, where each syringe is filled with a component of the gel-forming system. Adjusting the flow rates of the syringes so as to mix the components directly in the tube to the desired percentage, we were able to clearly define the zero-time of the experiment.

In this example, one of the syringes was filled with a suspension of PMMA particles in decalin, the other one with a suspension of polystyrene in decalin.

Soon after mixing, the presence of free polymers in the solvent triggers aggregation of particles by introducing new attractive forces: that is why this sample undergoes a gel-forming process (figure 5.4). Free non-adsorbing polymers added to the colloidal dispersion behave as random coils with a radius of gyration r_g. On average, they are excluded from a shell of thickness r_g around the colloidal particle, called the depletion zone. When two colloidal particles are brought together, these depletion zones overlap and the total volume accessible for the polymers increases. The free volume entropy of the system increases, and therefore aggregation is thermodynamically eased. This is the so-called depletion force. The range of the attraction is directly
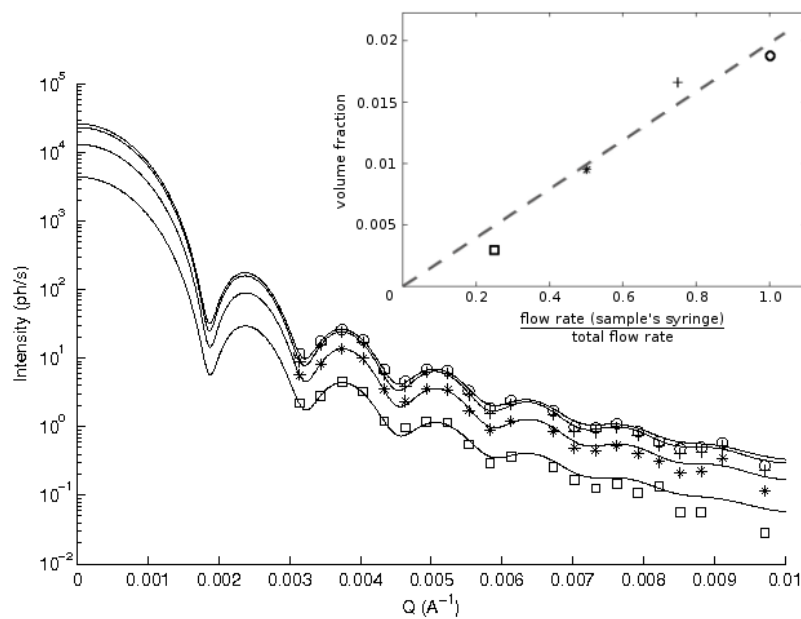

Figure 5.3: Silica particles in water droplets: SAXS measurements at different flow rates. In the smaller frame it is reported the volume fraction obtained from fitting as a function of silica particles' flow rate.
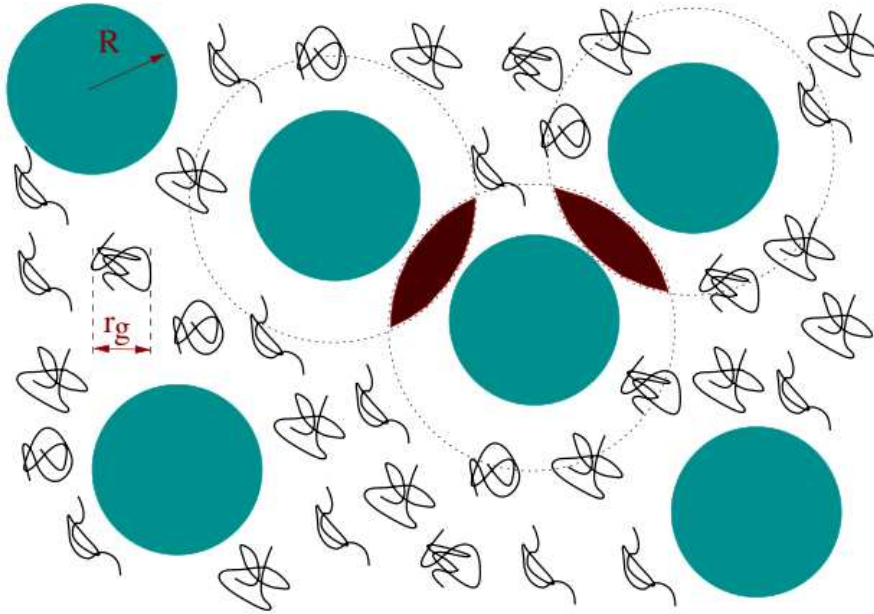
Figure 5.4: PMMA hard spheres, sterically stabilized, and polystyrene in decalin. Depletion force leads to gel formation.

related to the radius of gyration , whereas the strength is proportional to the osmotic pressure of the polymers.

The correlation functions were measured at different positions along the tube with known distances from the components mixing point $z0$, labelled from $z1$ to $z4$, as presented in figure 5.5. Only exchanged momentum $\vec{Q}$ perpendicular to the flow direction is considered. As it was for $\Phi \simeq 50\%$ sample (figure 4.18), the gel formation hinders the dynamics of the system. We observed a change in correlation functions with respect to the simple exponential form of equation 2.25. In literature, this correlation functions are usually fitted with a "stretched" exponential,

$$g^{(2)} = 1 + \exp(-2\Gamma t)^{\gamma}. \tag{5.1}$$

We can detect deviation from the hard-sphere behaviour simply looking at the two fitting parameters: particles moving in a Brownian way present $\Gamma \propto Q^2$ and $\gamma = 1$. In figure 5.6 and 5.7, Γ and γ as functions of the exchanged
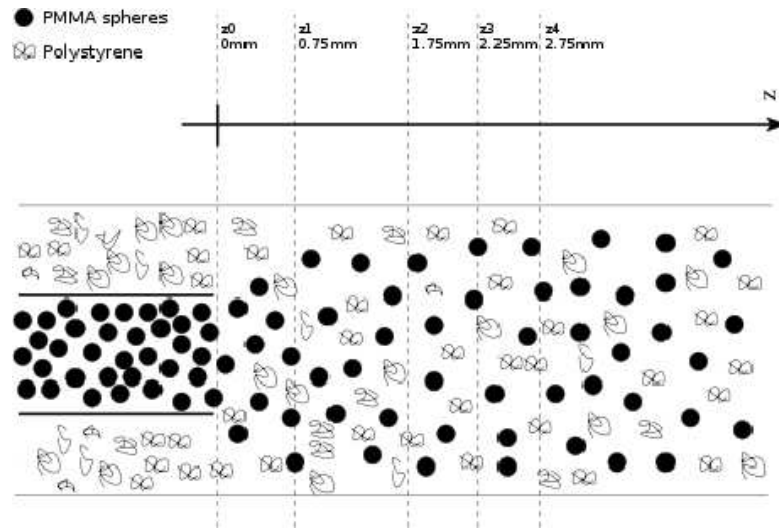
Figure 5.5: PMMA hard spheres, sterically stabilized, and polystyrene in decalin. SAXS patterns and correlation functions are measured at different beam positions along the tube.

momentum are reported, measured a couple of hours after the beginning of the flow experiment in position $z1$ and $z4$.
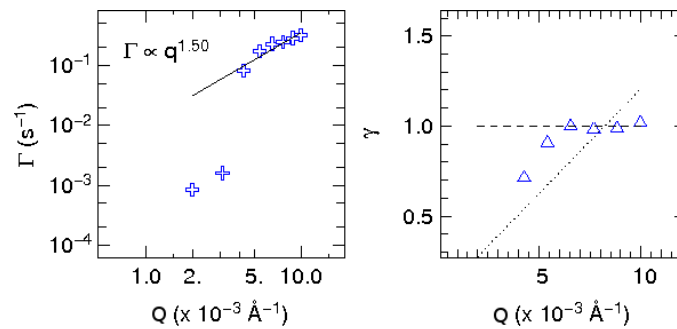

Figure 5.6: Stretched exponential parameters $\Gamma(Q)$ and $\gamma(Q)$ detected with beam position at $0.75mm$ from the point where the components of the gel are mixed.

The most evident change detected in correlation functions is related to the Γ parameter. Its Q dependence decays from the parabolic behaviour
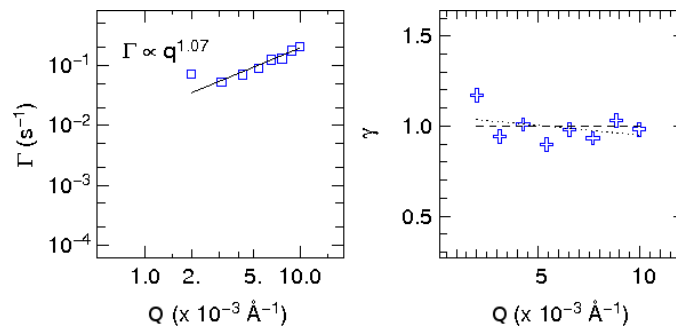
Figure 5.7: Stretched exponential parameters $\Gamma(Q)$ and $\gamma(Q)$ detected with beam position at $2.75mm$ from the point where the components of the gel are mixed.

characteristic of Brownian motion to a linear one while gel formation takes place. The meaning of this hyperdiffusive behaviour is still controversial. Some studies suggest a relaxation rate $\Gamma \propto Q^1$ which corresponds, in real space, to a mean square displacement $<\delta x^2>$ of a particle proportional to t^2 - where t is the elapsed time - and not to t^1, as in Brownian motion. In literature, some scientists tend to associate this hyperdiffusive behaviour to "jamming".

One big problem we experienced with gel forming directly into the tube is the possible occlusion of the tube. Due to this, the measurement had to be interrupted and the tube replaced. An example is reported in figure 5.8.

The microfluidics three-syringes configuration allows XPCS measurements on flowing droplets of sample, preventing the obstruction of the tube: the unique requirement is the measurement time, related to the motion of the droplets, being longer than the dynamics characteristic time. Creating longer droplets is a possible way to increase the measurement time without decreasing too much the velocity of the droplets, since a too low flow rate may lead to cavitation effects. Measuring the dynamics of a colloidal system in a droplet is a task that can not be accomplished without some previous considerations: we do not know if in the droplet the colloidal particles behave as in the bulk. They could move towards the surface, or the surface could
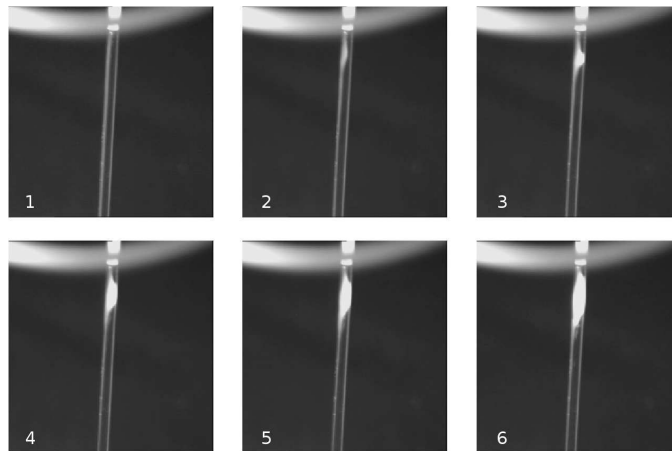
Figure 5.8: Uncontrolled gel formation. The tube is completely obstructed.

modify the dynamics. These tasks could be part of a basic agenda for future work.

Chapter 6

Conclusions

During several experimental sessions at ID10A, ESRF, we observed, on a system consisting of PMMA stabilized particles in decalin, the expected hard-sphere behaviour, at different concentrations from roughly 30% up to around 50%. We were able to measure the so-called hydrodynamic function $H(Q)$ and to compare it to theoretical models.

By means of SAXS we measured, initially, the characteristics of the sample, like particle radius, sample concentration and polydispersity, then we obtained information about inter-particle interactions from the Static Structure Factor $S(\Phi, Q)$. The $S(\Phi, Q)$ dependence from both the volume fraction of the sample Φ and the exchanged momentum Q is in good agreement with what is expected from the Percus-Yevich hard-sphere model.

A statistical analysis of XPCS led to an analytical, although approximated, expression for the standard deviation of the intensity-intensity correlation function. This was necessary in order to achieve a complete quantitative measurement. We concentrated our efforts on the dynamics that takes place during the time a particle needs to diffuse over a distance comparable with its radius.

The Stokes-Einstein's diffusion coefficient D_0 was measured by Dynamic Light Scattering, characterizing particle Brownian motion in low-concentration samples.

In order to avoid cavitation induced by the X-ray beam, the experiments were carried out with the sample flowing in a microfluidic device: keeping the exchanged momentum Q perpendicular to the flow and using low flow rates, we avoided any flow-induced effect over the measured quantities. While developing the necessary theory and all the experimental devices, we explored qualitatively other opportunities opened by the use of microfluidics in X-ray studies, like time-resolved studies or measurements in a confined volume.

In samples with higher volume fraction, the diffusion coefficient $D_S(Q)$ was measured by XPCS: it was no longer constant, since it showed an oscillatory behaviour analogous to that of the structure factor. Moreover, $D_S(Q)$ has a minimum in correspondence of the structure peak: this effect is the so-called "de Gennes narrowing". Trying to set aside the influence over dynamics given by the direct inter-particle interactions, we multiplied the measured diffusion coefficient by $S(Q)$, obtaining a function which in principle contains every other possible dependence from the exchanged momentum. We noted that H(Q) was in line with the one obtained from a model by Beenakker and Mazur [7] that takes into account the interactions mediated by the solvent in which the particles are suspended.

In high-concentration arrested regime, $D_S(Q)$ was sensibly smaller than its expected value for the "sol" regime/state: when the volume fraction was close to 50% the dynamic started to arrest, the sample looked like a gel and therefore the measured $H(Q)$ was totally different from the expected one.

Bibliography

[1] E. R. Weeks. *"Soft jammed materials" in Statistical Physics of Complex Fluids*, pages 2–87. S Maruyama & M Tokuyama (Tohoku University Press, Sendai, Japan), 2007.

[2] Tedpella Inc. (azienda produttrice di strumenti scientifici per la microscopia). http://www.tedpella.com/gold_html/goldsols.htm.

[3] M. Jenkins. *Quantitative Confocal Microscopy of Dense Colloidal Systems*. Ph.D. Thesis, University of Edinburgh, 2005.

[4] W. L. Griffith, R. Triolo, and A. L. Compere. Analytical scattering function of a polydisperse percus-yevick fluid with schulz (gamma) distributed diameters. *Phys. Rev. A*, 35(5):2200–2206, Mar 1987.

[5] P. N. Segrè, O. P. Behrend, and P. N. Pusey. Short-time brownian motion in colloidal suspensions: Experiment and simulation. *Phys. Rev. E*, 52(5):5070–5083, Nov 1995.

[6] C. W. J. Beenakker and P. Mazur. Self-diffusion of spheres in a concentrated suspension. *Physica A Statistical Mechanics and its Applications*, 120:388–410, July 1983.

[7] C. W. J. Beenakker and P. Mazur. Diffusion of spheres in a concentrated suspension II. *Physica A Statistical Mechanics and its Applications*, 126:349–370, July 1984.

[8] P. G. De Gennes. Liquid dynamics and inelastic scattering of neutrons. *Physica*, 25:825–839, January 1959.

[9] P. N. Pusey. *Liquid, Freezing and Glass Transition*, pages 805–820. D. Levesque and J. Zinn-Justin, Elsevier, Amsterdam, 1991.

[10] C. E. Williams. *Small Angle Scattering from solids and solutions, in Neutron and Synchrotron radiation for Condensed Matter studies, Hercules Course*, chapter 10. Baruchel et al., 1994.

[11] T. Narayanan. *Synchrotron small-angle X-ray scattering, in Soft Matter: Scattering, Imaging and Manipulation, Vol III*, chapter 8. R. Borsali and R. Pecora (Springer), 2007.

[12] Michael Kotlarchyk and Sow-Hsin Chen. Analysis of small angle neutron scattering spectra from polydisperse interacting colloids. *The Journal of Chemical Physics*, 79(5):2461–2469, 1983.

[13] Joachim Wagner. Small-angle scattering from spherical core–shell particles: an analytical scattering function for particles with Schulz–Flory size distribution. *Journal of Applied Crystallography*, 37(5):750–756, Oct 2004.

[14] M. Sutton, S. G. J. Mochrie, T. Greytak, S. E. Nagler, and L. E. Berman. Observation of speckle by diffraction by coherent X-rays. *Nature*, 352:608–610, aug 1991.

[15] Mark Sutton. A review of X-ray intensity fluctuation spectroscopy. *Comptes Rendus PhysiqueIn Press*, oct 2007.

[16] Gregory Brown, Per Arne Rikvold, Mark Sutton, and Martin Grant. Evolution of speckle during spinodal decomposition. *Phys. Rev. E*, 60(5):5151–5162, Nov 1999.

[17] ID10A beamline website. http://www.esrf.fr/UsersAndScience/ Experiments/SCMatter/ID10A.

[18] K. Schatzel, M. Drewel, and S. Stimac. Photon correlation measurements at large lag times: Improving statistical accuracy. *Journal of Modern Optics*, 35:711–718(8), April 1988.

[19] Saveez Saffarian and Elliot L. Elson. Statistical Analysis of Fluorescence Correlation Spectroscopy: The Standard Deviation and Bias. *Biophys. J.*, 84(3):2030–2042, 2003.

[20] E. Jakeman. *Photon Correlation and Light Beating Spectroscopy*, pages 116–121. Plenum, New York, 1973.

[21] P. Falus, L. B. Lurio, and S. G. J. Mochrie. Optimizing the signal-to-noise ratio for X-ray photon correlation spectroscopy. *Journal of Synchrotron Radiation*, 13(3):253–259, May 2006.

[22] D. Lumma, L. B. Lurio, S. G. J. Mochrie, and M. Sutton. Area detector based photon correlation in the regime of short data batches: Data reduction for dynamic x-ray scattering. *Review of Scientific Instruments*, 71(9):3274–3289, 2000.

[23] P. N. Pusey and W. Van Megen. Phase behaviour of concentrated suspensions of nearly hard colloidal spheres. *Nature*, 320:340–342, March 1986.

[24] S. Busch, T. H. Jensen, Y. Chushkin, and A. Fluerasu. Dynamics in shear flow studied by X-ray Photon Correlation Spectroscopy. *European Physical Journal E*, 26:55–62, May 2008.

Ringraziamenti